QUANTUM MONTE CARLO STUDY OF SEMICONDUCTOR ARTIFICIAL GRAPHENE NANOSTRUCTURES

A Thesis Submitted to
the Graduate School of
İzmir Institute of Technology
in Partial Fulfillment of the Requirements for the Degree of

DOCTOR OF PHILOSOPHY

in Physics

by
Gökhan Öztarhan

July 2025
İZMİR

We approve the thesis of **Gökhan Öztarhan**

Examining Committee Members:

Prof. Dr. A. Devrim Güçlü
Department of Physics, İzmir Institute of Technology

Doç. Dr. Özgür Çakır
Department of Physics, İzmir Institute of Technology

Doç. Dr. Mehmet Yağmurcukardeş
Department of Photonics, İzmir Institute of Technology

Prof. Dr. Ramazan Tuğrul Senger
Department of Physics, İzmir University of Economics

Prof. Dr. Hâldun Sevinçli
Department of Physics, Bilkent University

04/07/2025

Prof. Dr. A. Devrim Güçlü
Supervisor, Department of Physics
İzmir Institute of Technology

Prof. Dr. Lütfi Özyüzer
Head of the Department of
Department of Physics

Prof. Dr. Mehtap Eanes
Dean of the Graduate School of
İzmir Institute of Technology

ACKNOWLEDGMENTS

I would like to thank my supervisor Prof. Dr. A. Devrim Güçlü for his academic guidance, encouragement, patience, understanding and friendship throughout my PhD study. I consider myself fortunate to have studied under his mentorship. His support made it possible for me to embark on this Ph.D. journey, and I am deeply grateful to him for providing me with this invaluable opportunity.

I am thankful to the committee members of my thesis Doç. Dr. Özgür Çakır, Doç. Dr. Mehmet Yağmurcukardeş, Prof. Dr. Ramazan Tuğrul Senger and Prof. Dr. Hâldun Sevinçli for their valuable time, participation and proofreading.

I am deeply grateful to my dearest wife, İdem Susuzlu Öztarhan, for walking beside me through every step of this journey, especially during the most difficult days of my life. Her endless love, patience, and unwavering support gave me the strength to keep going, and made this achievement possible.

I would like to thank my colleagues for valuable discussions.

I am also thankful to my family for their endless support.

This work was supported by The Scientific and Technological Research Council of Turkey (TUBITAK) under the 1001 Grant Project Number 119F119. The numerical calculations reported in this study were partially performed at TUBITAK ULAKBIM, High Performance and Grid Computing Center (TRUBA resources).

ABSTRACT

QUANTUM MONTE CARLO STUDY OF SEMICONDUCTOR ARTIFICIAL GRAPHENE NANOSTRUCTURES

Semiconductor-based artificial graphene nanostructures provide a highly tunable platform for exploring strongly correlated quantum phases, with Hubbard model interaction strengths reaching $U/t \sim 100$. In this thesis, we employ high-precision variational and diffusion Monte Carlo methods to study magnetic and metal-insulator transitions in finite-sized honeycomb lattices nanopatterned on GaAs quantum wells.

We demonstrate a transition from antiferromagnetic to metallic phases as a function of lattice site radius ρ, for a fixed lattice constant $a = 50$ nm and electron numbers up to 114. By analyzing spin-spin correlation functions in hexagonal flakes with armchair edges, we find that system geometry and charge nonuniformity significantly affect the steepness and critical point of the phase transition.

In addition, we report the emergence of Nagaoka ferromagnetism in these armchair-edged hexagonal structures under realistic long-range Coulomb interactions. A magnetic phase transition is induced by the addition or removal of a single electron at half-filling, providing a clear signature of itinerant ferromagnetism predicted by the Hubbard model. These findings offer insight to experimental studies by demonstrating the feasibility of observing such magnetic phases in large-scale, physically realistic systems at interaction strengths near $U/t \approx 60$.

ÖZET

YARI İLETKEN YAPAY GRAFEN NANOYAPILARIN KUANTUM MONTE KARLO İLE İNCELENMESİ

Yapay yarıiletken grafen nanoyapıları, $U/t \sim 100$ mertebesine ulaşabilen Hubbard modeli etkileşim gücüyle, güçlü korelasyonlu kuantum fazlarının incelenmesi için son derece ayarlanabilir bir platform sunmaktadır. Bu tezde, GaAs kuantum kuyularına nanopattern edilmiş sonlu boyutlu bal peteği örgülerinde manyetik ve metal-yalıtkan geçişlerini incelemek amacıyla yüksek hassasiyetli varyasyonel ve difüzyon Monte Carlo yöntemleri kullanılmaktadır.

Sabit örgü sabiti $a = 50$ nm ve 114'e kadar elektron sayısı için, örgü nokta yarıçapı ρ'ya bağlı olarak antiferromanyetikten metale bir faz geçişi gösterilmektedir. Kol tipi (armchair) kenarlı altıgen pullarda spin-spin korelasyon fonksiyonları analiz edilerek, sistem geometrisi ve yük homojensizliğinin geçişin keskinliği ve kritik noktası üzerinde belirgin etkileri olduğu ortaya konmaktadır.

Ayrıca, uzun menzilli Coulomb etkileşimleri altında, bu kol kenarlı altıgen yapılarda Nagaoka ferro-manyetizmasının ortaya çıktığı gösterilmektedir. Yarı dolulukta bir elektronun eklenmesi veya çıkarılmasıyla tetiklenen manyetik faz geçişi, Hubbard modeli tarafından öngörülen gezici (itinerant) ferro-manyetizmanın açık bir göstergesidir. Bulgularımız, $U/t \approx 60$ civarında bu tür manyetik fazların büyük ölçekli ve fiziksel olarak gerçekçi sistemlerde gözlemlenebilirliğini göstererek deneysel çalışmalara önemli bir katkı sunmaktadır.

TABLE OF CONTENTS

LIST OF FIGURES

Figure **Page**

LIST OF ABBREVIATIONS

AG . . . . . Artificial Graphene
QMC . . . . . Quantum Monte Carlo
Fig. . . . . Figure
VMC . . . . . Variational Monte Carlo
DMC . . . . . Diffusion Monte Carlo
DFT . . . . . Density Functional Theory
TB . . . . . Tight-binding
MFH . . . . . Mean-field Hubbard
FM . . . . . Ferromagnetic
AFM . . . . . Antiferromagnetic
SPSE . . . . . single-particle Schrödinger equation

CHAPTER 1

INTRODUCTION

Graphene is a two-dimensional material made of carbon atoms on a honeycomb lattice structure. Thanks to its linear energy dispersion near Fermi level, graphene has interesting electronic, optical and thermal properties leading it to be one of the most investigated materials in the last several decades.[1–11] However, the fabrication and reliability issues of nanostructured graphene, such as graphene quantum dots, make it harder to observe many interesting phenomena.[12–14] In recent years, technological advancement in artificial superlattices gives us opportunity to develop practical quantum simulators.[15,16] Not only they allow us to replicate complex systems being hard to fabricate, but also they provide us testing environments to verify theoretical predictions. In this respect, artificial graphene (AG) nanostructures, designed by imitating the 2D honeycomb pattern of graphene, have been proven to be good candidates for being more reliable and controllable sources for both fabrication and investigation of many physical phenomena.[16] AG nanostructures can be formed using semiconductor materials or optical lattices. In this study, we cover the semiconductor AG nanostructures, formed by nanopatterned GaAs quantum wells.

In the last decade, even though theoretical predictions for AG nanopatterned on 2D electron gas show strong electron localizations in the quantum dots, experimental realization of graphenelike behavior of modulation-doped AlGaAs/GaAs quantum wells was not clearly present until the lattice constant of honeycomb array shrinking down to approximately 50 nm (and confinement potential radius around 7.5 - 17.5 nm).[16–20] Observation of Dirac fermions in AG nanostructures provides new opportunities for studying graphene quantum dots. AG offers tunability of the system parameters (such as lattice constant, site radius or potential depth) while overcoming the fabrication and reliability issues (e.g. presence of impurities) of ”real” graphene quantum dots. Emergence of Dirac bands at smaller lattice periods, however, may indicate a strong electron correlation behavior, and even existance of different quantum phases depending on quantum well radius or the lattice constant itself. Studies on real graphene quantum dots, which predict several

electronic and magnetic phases depending on geometry of graphene flakes[11], are also a concrete background for the possible existence of these phases in AG quantum dots.

Extensive tunability of the AG nanostructures allows the control of interactions between the electrons and tunneling strength between sites. Therefore, the Hubbard parameter U/t can be tuned using the basic parameters of AG. In experimental structures with a lattice constant $a = 50$ nm[16], U/t can have values as high as 350 (discussed in chapter 5), which is two orders of magnitude larger than the critical value for the antiferromagnetic Mott transition predicted by calculations based on the Hubbard model for a honeycomb lattice.[21–24] Additionally, long-range electron repulsion does not cancel the attraction of the artificial confining potential in AG even near charge neutrality, unlike in real graphene (in real graphene attraction potential of the sites and the electron repulsion have the same functional form, i.e. Coulomb interactions between electron and the site, or between the electrons). For such significant and long-ranged electron interactions, a non-perturbative many-body approach is necessary to accurately account for the correlation effects.

Earlier theoretical studies using density functional theory (DFT) and path integral Monte Carlo calculations showed that Dirac bands are stable against electron interaction effects.[18,19] Recent works on triangular zigzag geometry with lattice constant $a = 12.5 - 15$ nm predict an antiferomagnetic (AFM) insulator to metallic transition using Hartree-Fock and exact diagonalization calculations which also emphasize the effects of electron correlations in AG systems.[25]

Although DFT, tight-binding (TB) and mean-field Hubbard (MFH) methods can provide basic insight about AG quantum dots, electron-electron interactions should be treated more carefully in the presence of a strong electron correlation regime. Hence, we present variational Monte Carlo (VMC) and diffusion Monte Carlo (DMC) calculations for non-perturbative and accurate treatment of electron correlations within the fixed-node approximation.[26–31] Convenience of these quantum Monte Carlo (QMC) methods is to examine the systems in real-space and to be able to alter the system parameters without limitations. We examine the behavior of AG quantum dots under varying dot radius while keeping the system charge neutral and extract detailed electron density and spin-spin correlation information in real-space.

Our modelling of nanostructured AG on the modulation-doped AlGaAs/GaAs

quantum wells consists of N_e interacting electrons in a honeycomb array of N confining potentials, described by the many-body Hamiltonian in effective atomic units (electronic charge e, dielectric constant ϵ, effective mass m^*, and $\hbar$ are set to 1, see Appendix E for conversion to atomic units)

$$H = -\frac{1}{2}\sum_{i}^{N_e}\nabla_i^2 + \sum_{i}^{N_e}V(\mathbf{r}_i) + \sum_{i}^{N_e}k|\mathbf{r}_i|^2 + \sum_{i<j}^{N_e}\frac{1}{r_{ij}} \tag{1.1}$$

where $1/r_{ij}$ is the Coulomb interaction between the electrons, $V(\mathbf{r}_i)$ is the total potential energy of the confining potentials, and k is the spring constant of quadratic gate potential that is located at the center of the system which controls the finite size effects (k can be interpreted as control switch of gate potential, as well.). Typical material properties for GaAs, effective electron mass $m^* = 0.067m_0$ and dielectric constant $\epsilon = 12.4$, are used.[17,32] Corresponding effective Bohr radius is $a_0^* = 9.793728$ nm, and the effective Hartree energy is 11.857199 meV. Honeycomb lattice structure is formed by quantum dots potentials using gaussian-like functions[20,33],

$$V(\mathbf{r}) = V_0\sum_{\mathbf{R}_0}\exp[-(|\mathbf{r}-\mathbf{R}_0|^2/\rho^2)^s] \tag{1.2}$$

where $s \geq 1$, V_0 is the potential depth, ρ is the radius and s is the sharpness of the potential wells, as in Fig. 1.1. $\mathbf{R}_0$ is the location of the potential wells.

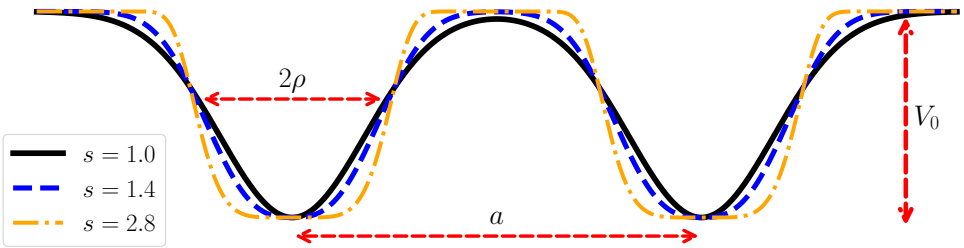

Figure 1.1. The form of the potential wells.

In our numerical calculations revealing metallic to AFM transition, $N_e = N$ electrons are considered. The dot-to-dot distance is fixed to $a = 50$ nm (as in experimental

studies) while several radius values from $\rho = 10$ nm to $\rho = 35$ nm are covered. Three different sharpness values are used to cover both gaussian-like smooth shapes and sharp muffin-tin like shapes since the functional shape of the potential wells can vary depending on the sample quality. The sharpness values used in simulations are $s = 1$ for smoothly changing gaussian-like potential wells, $s = 2.8$ for sharp muffin-tin like potentials and $s = 1.4$ for the potential shapes in between. V_0 values vary depending on dot radius (increasing from -42 meV to -15 meV, approximately linear for increasing dot radius) to keep the total energy of the system close to zero, since our aim is to imitate the charge neutral behavior of graphene. Our system is an hexagonal flake with armchair edges geometry. We consider two system sizes; one of them has 42 sites and 42 electrons, and the other one consists of 114 sites and 114 electrons. Fig. 1.2 shows an example of 42 confinement potentials on the honeycomb lattice. The overlap between the quantum dot potentials can be controlled by changing the radius ρ of the potential wells as seen in Fig. 1.3. In Fig. 1.4, 114 quantum dots on hexagonal armchair flake is shown.

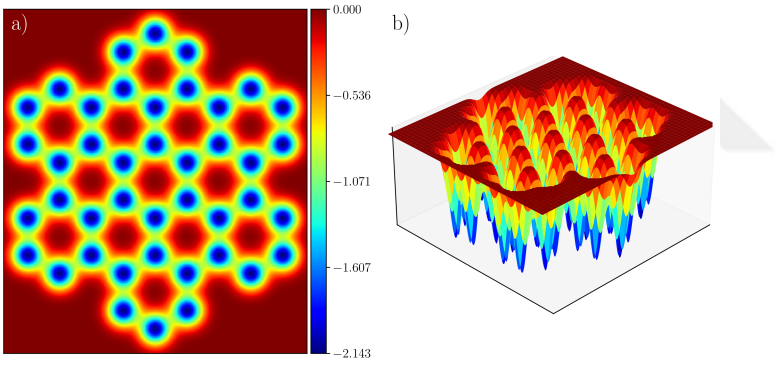

Figure 1.2. Quantum dots on honeycomb lattice for an hexagonal flake with armchair edges. a) 2D mesh of potential, colorbar shows the value of the potential V on real space. b) 3D projection of the potential on the lattice.

Moreover, we also predict that Nagaoka ferromagnetism can be probed in semiconductor AG systems.[34] Recent advancements in these systems have enabled the precise manipulation of correlated insulating phases and emergent magnetism[25,33], opening pathways to the experimental realization of exotic quantum effects, including Nagaoka ferromagnetism. Originally predicted within the framework of the strongly correlated Hubbard model[35,36] (see Appendix F), Nagaoka ferromagnetism arises from a mechanism wherein

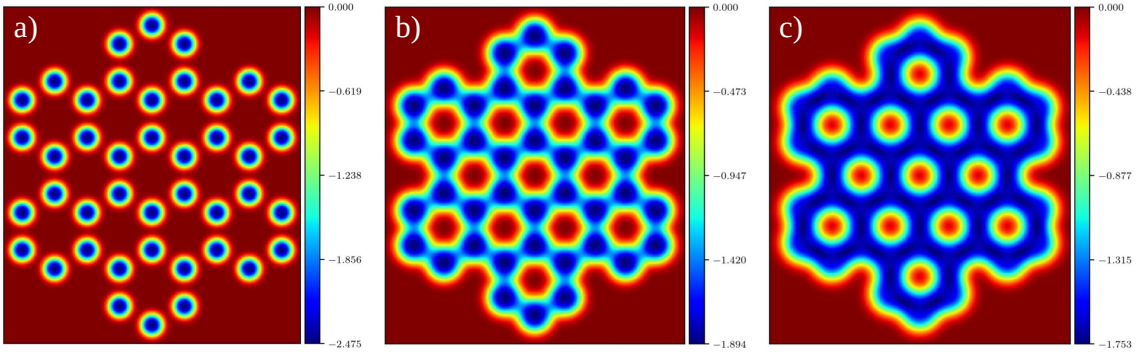

Figure 1.3. Quantum dots on armchair hexagonal flake with 42 sites using different ρ values. Dot-to-dot distance $a = 50$ nm. V_0 values are choosen for charge-neutral system. a) $\rho = 15$ nm. b) $\rho = 25$ nm. c) $\rho = 30$ nm.

a single hole in a half-filled lattice induces a fully spin-polarized state-an effect that remains elusive in conventional materials due to disorder and competing interactions. AG, with its highly tunable electron filling, interaction strength, and band structure, provides an ideal platform for probing this phenomenon under well-controlled conditions, potentially enabling the first direct realization of itinerant ferromagnetism in a programmable quantum system. Recent observations of Nagaoka ferromagnetism across various lattice geometries further reinforce the prediction that it can be realized in AG systems.[37–39] Nagaoka ferromagnetism was investigated within Hubbard model for a single hole for finite and infinite-U limit, and with different hole densities[40–46], extended Hubbard model[47,48] and ab initio exact diagonalization[49] for small size systems. Whether Nagaoka ferromagnetism can be realized in larger scale solid-state systems remains an open question as Coulomb interactions include not only finite on-site repulsion but also long-range and scattering terms.[50] In this work, we present computational calculations to investigate the emergence of Nagaoka ferromagnetism in semiconductor-based AG, leveraging its controllable electronic structure and interaction-driven phase transitions. Our findings not only deepen the fundamental understanding of strongly correlated electrons in synthetic lattices but also establish a framework for engineering novel quantum magnetic phases in artificial quantum materials.

In the numerical calculations revealing the Nagaoka ferromagnetism transition, dot-to-dot distance is fixed to $a = 50$ nm, while two radius values $\rho = 17.5$ nm to 25 nm is considered. The sharpness value s is fixed, as well, to $s = 1.4$ which is the

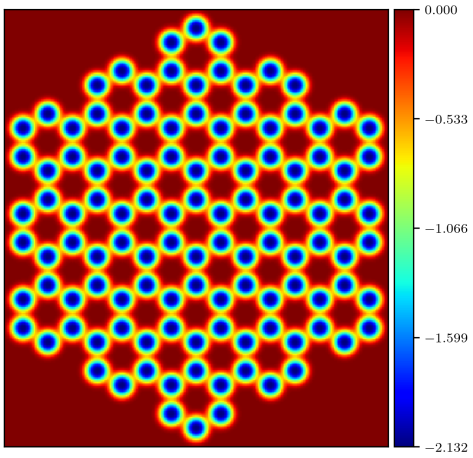

Figure 1.4. Quantum dots on armchair hexagonal flake with 114 sites for $\rho = 20$ nm. Dot-to-dot distance $a = 50$ nm.

intermediate point between gaussian ($s = 1$) and muffin-tin like ($s = 2.8$) potentials.[33] V_0 values increasing monotonically from -5 meV to -40 depending on dot radius and the transition point. A single number of potential wells is considered, $N = 42$. The corresponding number of electrons is chosen for half-filling ($N_e = 42$) and exactly one hole away from half-filling ($N_e = 41$). The spring constant of the quadratic gate potential is kept constant during all calculations which eliminates finite size effects, $k = 3.56 \times 10^{-4}$ meV/nm^2.[33]

CHAPTER 2

METHODOLOGY

Our aim is to calculate electronic and magnetic properties in the ground state. In order to estimate ground state properties, variational and diffusion Monte Carlo methods are used. Both methods use trial wave functions to obtain the ground state properties of the system but with different approaches. In this chapter, we explain the VMC and DMC methods in detail, describe the preparation of the trial wave functions used in these methods. The orbitals in the Slater determinants of trial wave functions is prepared using a diagonalization of TB and MFH Hamiltonian, and we explain how to predict the hopping parameter, t, and onsite Coulomb interaction, Hubbard U.

2.1. Variational Monte Carlo

In VMC method[26,27], a trial wave function is constructed with tunable parameters. Then, the tunable parameters of trial wave function is optimized using variational principle. Variational principle states that expectation value of the energy using any normalizable function Ψ_T gives an upper bound to the ground state energy, E_0, as shown in equation 2.1.

$$E_V = \frac{\langle \Psi_T(\alpha)|\hat{H}|\Psi_T(\alpha)\rangle}{\langle \Psi_T(\alpha)|\Psi_T(\alpha)\rangle} > E_0 \tag{2.1}$$

where α are the tunable parameters, $\alpha = (\alpha_1, \alpha_2, \alpha_3, ...)$. Using the derivatives of the variational energy E_V with respect to α as in equation 2.2, the trial wave function is optimized to give the minimum energy possible.

$$\frac{\partial}{\partial \alpha} E_V = 0 \tag{2.2}$$

Newton's method[51], which is one of the best optimization methods, is used to optimize the tunable parameters of the trial wave function.

Expectation value of Hamiltonian, however, is calculated using Monte Carlo integration methods[52–55] since it includes multi-dimensional integrals as following.

$$E_V = \frac{\int \Psi_T^*(\mathbf{R})\hat{H}\Psi_T(\mathbf{R})d\mathbf{R}}{\int \Psi_T^*(\mathbf{R})\Psi_T(\mathbf{R})d\mathbf{R}} \text{ where } \mathbf{R} = (\mathbf{r}_1\sigma_1, \mathbf{r}_2\sigma_2, ..., \mathbf{r}_N\sigma_N) \tag{2.3}$$

for N electrons. Here, $\mathbf{r}_i$ and σ_i are the position and the spin of the i^{th} electron respectively.

2.2. Diffusion Monte Carlo

DMC method[28,29] calculates a mixed expectation value of energy using the trial wave function and the exact wave function of the Hamiltonian as in equation 2.4.

$$E_0 = \frac{\langle \Psi_0 | \hat{H} | \Psi_T \rangle}{\langle \Psi_0 | \Psi_T \rangle} \tag{2.4}$$

where E_0 is the exact ground state energy and Ψ_0 is the exact ground state wave function. Here, the unknown ground state wave function, Ψ_0, is obtained through a projection method. The imaginary-time evolution of trial wave function is calculated using the Hamiltonian of the system in order to project out the ground state function. The imaginary-time evolution of trial wave function is following.

$$|\Psi_T(\tau)\rangle = e^{-(\hat{H}-E_T)\tau}|\Psi_T\rangle \tag{2.5}$$

where τ is the negative imaginary time, $\tau = -it$, and E_T is the trial energy. By decomposing the trial wave function using the exact eigenstates of the Hamiltonian, one can easily show that in the limit of infinite propagation time, the resulting wave function is dominated by the ground state wave function (or the lowest eigenstate which have nonzero

overlap with trial wave function).

$$\lim_{\tau\to\infty} |\Psi_T(\tau)\rangle \approx e^{-(E_0-E_T)\tau}|\Psi_0\rangle\langle\Psi_0|\Psi_T\rangle \tag{2.6}$$

Since all energies greater than the ground state energy decay exponentially faster, the resulting wave function is proportional to the exact ground state wave function. By tuning trial energy, convergence to the ground state can be guaranteed as long as the trial wave function have an overlap with the ground state.

$$\lim_{\tau\to\infty} |\Psi_T(\tau)\rangle \approx |\Psi_0\rangle \tag{2.7}$$

Thus, using Green's function formalism, the imaginary time evolution of trial wave function is calculated through Monte Carlo methods in order to obtain the ground state properties of the systems.[31,56]

All computational methods have some advantages and drawbacks depending on where we use them, and QMC methods are no different. Firstly, in both VMC and DMC methods, there is a controllable statistical error which is the nature of Monte Carlo integration. Since values of interest are calculated through random sampling from configuration spaces (or integration domains), the results have a statistical error, however it can be completely controlled by increasing the number of samples in both VMC and DMC. Secondly, in VMC the resulting wave function is extremely dependent on the trial wave function. The more flexible tunable parameters introduced in trial wave function, the closer expectation value of energy to the ground state energy. This problem can be solved by introducing DMC since it projects out the exact ground state of the system. Generally, the optimized wave function via VMC methods is used as a starting point (trial wave function) for DMC methods. Thirdly, in DMC in order to progress in the imaginary-time and to use Green's function formalism, imaginary-time domain is split into small-time intervals (Trotter-Suzuki decomposition), which introduces a time step error that can be easily controlled by setting imaginary-time steps small. Another issue is that calculation of Green's functions using Monte Carlo method introduces a weighted random walk in the configuration space in which the weights can have large fluctuations depending on

the problem. The averages can be dominated by the random samples with large weights and this causes inefficiencies in the algorithm.[31,56] In order to overcome this issue, a population of walkers is introduced in contrast to VMC in which the random samples are obtained from a single walker. The population of walkers produce a population error in the end result yet it can be also controlled easily by increasing the number of walkers in the population. The errors we have mentioned so far can be completely controllable and do not raise an issue for our calculations. Nevertheless, similar to all projector Monte Carlo methods, DMC method also suffers from notorious fermion sign problem. There are several interpretations of sign problem.[31,56] Algorithm converges to bosonic state of lower energy instead of the fermionic state, or even if fermion symmetry is imposed to the wave function, negative weights appear in the simulation and the computation time increases exponentially because of cancellations. In order to avoid sign problem, fixed node approximation[31,56] is used in DMC calculations in which the resulting wave function is forced to have same nodal structure as those of the trial wave function. If the nodal structure of trial wave function is same as nodal structure of the exact ground state of the system, the DMC results become exact. Thus, the quality of the nodal structure of the trial wave function affects the accuracy of the DMC results. This solution introduces the fixed node approximation error which is the only uncontrollable error in our method. However, we can overcome this issue by preparing good quality trial wave functions via VMC.[57]

2.3. Trial Wave Functions

Accuracy of the simulations depends on trial wave functions in both VMC and DMC methods. We first perform VMC calculations to optimize the nodal structure of the trial wave function, providing an upper bound to the ground state energy. After that DMC calculations project out the ground state in the fixed node approximation. In order to start with the most flexible wave function possible, Slater-Jastrow trial wave functions are used along with the advanced optimization techniques, and they have the following form.

$$\Psi_T(\mathbf{R}) = e^{J(\mathbf{R})} D(\mathbf{R}) \tag{2.8}$$

where J is the Jastrow factor, D is the Slater determinant and $\mathbf{R} = (\mathbf{r}_1\sigma_1, \mathbf{r}_2\sigma_2, ..., \mathbf{r}_N\sigma_N)$. Jastrow factor consists of tunable parameters, and can be written as

$$J(\mathbf{R}) = \sum_i \chi(\mathbf{r}_i\sigma_i) + \frac{1}{2}\sum_{\substack{i,j \\ i\neq j}} u(\mathbf{r}_i\sigma_i, \mathbf{r}_j\sigma_j) + \frac{1}{2}\sum_{\substack{i,j \\ i\neq j}} u'(\mathbf{r}_i\sigma_i, \mathbf{r}_j\sigma_j) \tag{2.9}$$

where χ includes the electron-dot (or electron-nucleus for atomic systems) correlations, u is the electron-electron correlations, and u' includes three-body interactions such as electron-electron-dot correlations.[57–60] One example of u in Jastrow factor used to model homogeneous electron gas used by Ceperley in 1978[61] is the following.

$$u(\mathbf{r}_i\sigma_i, \mathbf{r}_j\sigma_j) = \frac{A_{\sigma_i\sigma_j}}{r_{ij}}(1 - e^{-r_{ij}/F_{\sigma_i\sigma_j}}) \tag{2.10}$$

where $A_{\sigma_i\sigma_j}$ and $F_{\sigma_i\sigma_j}$ are free parameters of the trial wave function, and wave function is optimized with respect to them.

Omitting spin indices, the Slater determinants can be written as

$$D(\mathbf{R}) = \frac{1}{\sqrt{N!}}\begin{vmatrix} \psi_1(\mathbf{r}_1) & \psi_2(\mathbf{r}_1) & \dots & \psi_N(\mathbf{r}_1) \\ \psi_1(\mathbf{r}_2) & \psi_2(\mathbf{r}_2) & \dots & \psi_N(\mathbf{r}_2) \\ \vdots & \vdots & \ddots & \vdots \\ \psi_1(\mathbf{r}_N) & \psi_2(\mathbf{r}_N) & \dots & \psi_N(\mathbf{r}_N) \end{vmatrix} \tag{2.11}$$

where ψ_n's can be either atomic or molecular orbitals.

In order to form Slater determinants, we prepare three different types of orbitals using localized gaussian functions that are proven to be one of the most suitable functions for 2D systems of quantum dots.[32,62,63] In the first method, localized gaussian functions, ϕ_m, are defined for each orbital on lattice sites ($\psi_1 = \phi_1$, $\psi_2 = \phi_2$, ..., $\psi_N = \phi_N$). Gaussian orbitals can describe strongly localized states more easily. In the other two methods, each orbital are constructed by a linear combination of localized Gaussian functions $\psi_n = \sum_i c_{ni}\phi_i$, where the coefficients c_{ni} are obtained from diagonalization of TB and MFH Hamiltonians. TB orbitals may be used to express unconfined states in which

electrons move more freely than gaussian orbitals. MFH orbitals, however, can describe both localized and unconfined states depending on the ratio of Coulomb interaction and the hopping parameter. Corresponding tight-binding Hamiltonian is

$$H_{TB} = -t \sum_{\langle i,j\rangle,\sigma} c^{\dagger}_{i\sigma} c_{j\sigma} + h.c. \tag{2.12}$$

and mean-field Hubbard Hamiltonian is

$$H_{MFH} = -t \sum_{\langle i,j\rangle,\sigma} c^{\dagger}_{i\sigma} c_{j\sigma} + U \sum_{i,\sigma} \langle c^{\dagger}_{i,-\sigma} c_{i,-\sigma}\rangle c^{\dagger}_{i\sigma} c_{i\sigma} + h.c. \tag{2.13}$$

where $c^{\dagger}$ (c) is the creation (annihilation) operator, t is the hopping parameter between nearest neighbor sites, U is the Coulomb interaction between the electrons in the same site, and $\langle i, j\rangle$ indicates the sum is over nearest neighbor indices. In order to extract diverse behavior of orbitals from MFH calculations, we use both $U = 2t$ and $U = 20t$ ratios for metallic and localized states.

2.4. Extrapolated Estimator

Although the ground state energy can be calculated by the mixed estimator of DMC algorithm, such as $E_{DMC} = \langle\psi_0|\hat{H}|\psi_T\rangle/\langle\psi_0|\psi_T\rangle$, an extrapolated calculation is required for the observables that do not commute with the Hamiltonian. In this study, all quantities that do not commute with the Hamiltonian are calculated with the extrapolated estimator

$$\langle\hat{O}\rangle = 2\langle\hat{O}\rangle_{DMC} - \langle\hat{O}\rangle_{VMC}. \tag{2.14}$$

2.5. Calculation of t and U

For calculations revealing metallic to AFM phase transition, the hopping parameter t is obtained from DFT calculations; band structure is obtained via DFT calculations of bulk artificial graphene. Slope of the band structure gives the hopping parameter t by the following formula.

$$t = \frac{2}{3a}\frac{dE}{dk} \tag{2.15}$$

where a is the lattice constant. Hubbard U is obtained from the solutions of Schrödinger's equation for a single quantum dot as in the following.

$$U = 2\pi \int rn(r)V_e(r)dr \tag{2.16}$$

where n is the density and V_e is the potential on the electron.

For calculations revealing Nagaoka ferromagnetism, the onsite Coulomb interaction, U, is determined using extrapolated electron densities from quantum Monte Carlo calculations of Sz-scanned systems of $N_e = 41$ electrons. Conversely, the nearest-neighbor hopping parameter, t, is estimated through a hybrid approach that combines solutions of the single-particle Schrödinger equation (SPSE) with the diagonalization of the TB Hamiltonian for an artificial benzene molecule in which $\rho = 17.5$ nm. The energy spectra obtained from SPSE solutions (Fig. 2.1a) and TB Hamiltonian (Fig. 2.1b) diagonalization are systematically compared and fitted. The hopping parameter, t, is subsequently extracted by iteratively adjusting and refining the TB model to achieve optimal agreement with the computed spectra (Fig. 2.1c).

2.6. Summary

In conclusion, we prepare trial wave functions with tunable parameters. The parameters of the trial wave functions are optimized using VMC method. DMC method

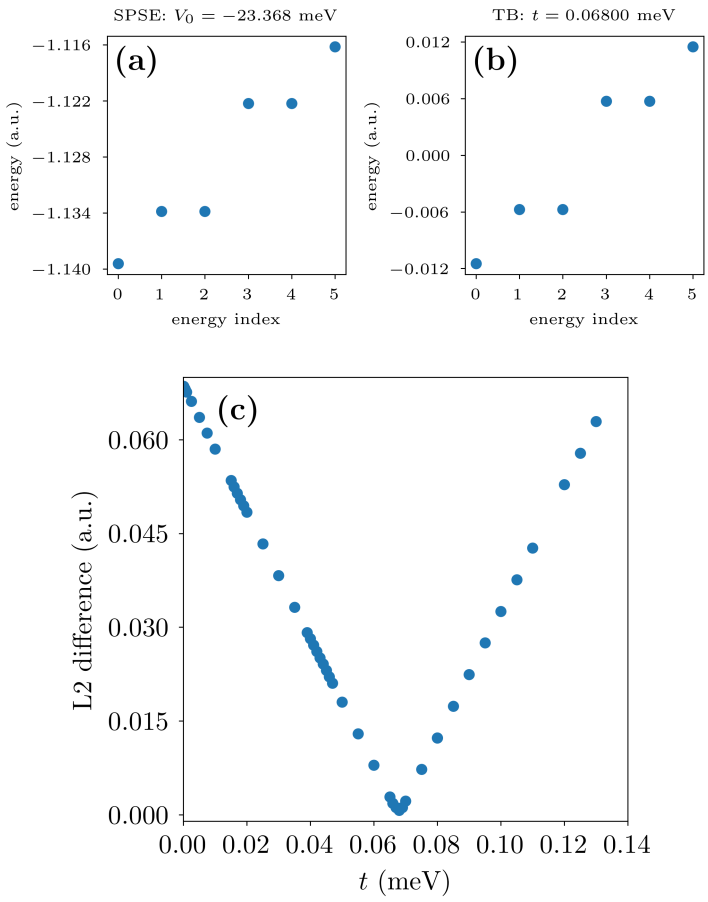

Figure 2.1. (a) SPSE solutions for $V_0 = -23.368$ meV. (b) TB energy spectra for $t = 0.068$ meV. (c) L2 difference between SPSE and TB spectra with respect to TB hopping parameter, t.

starts with the optimized trial wave functions, and extracts the ground state of the system using imaginary-time propagation, within fixed node approximation. Trial wave functions are prepared using localized Gaussian functions and their linear combinations in which the coefficients are obtained from TB and MFH methods. The hopping parameter t and Hubbard U are estimated using DFT, single particle Schrödinger equation and TB methods.

CHAPTER 3

CALCULATION OF PARAMETER DERIVATIVES FOR NON-DIAGONAL ORBITAL COEFFICIENT MATRICES

In order to minimize the energy or variance (or both) using VMC (as mentioned in Chapter 2 and equation 2.2), we have to calculate the derivatives of the expectation value of the variational quantity with respect to the free parameters (e.g. basis function and Jastrow factor parameters, determinant and configuration state function coefficients). In this chapter, we only consider the basis function parameters since the other parts of the program, with which we perform our calculations, are robust, yet similar calculations are valid for all free parameters. Since the calculation and implementation is not trivial, this chapter explain them in detail.

The main point is that for quantum dot systems, the previous implementation only considers diagonal orbital coefficient matrices (in which orbitals are represented by a single Gaussian basis function), and uses a trick using Sherman-Morrison formula to update the derivatives in the most efficient way. In this study, however, we also use a linear combination of Gaussian basis functions for forming the Slater matrices. Therefore, a different scheme is required to calculate the derivatives of the Slater matrices including the linear combinations of basis functions in its orbitals.

The expectation value of variational energy (using notation $\Psi \equiv \Psi_T$) is

$$\overline{E} = \frac{\langle \Psi | \hat{H} | \Psi \rangle}{\langle \Psi | \Psi \rangle} = \frac{\int \Psi^* \hat{H} \Psi d\mathrm{R}}{\int \Psi^* \Psi d\mathrm{R}} = \int \frac{|\Psi|^2}{\int |\Psi|^2 d\mathrm{R}} \frac{\hat{H}\Psi}{\Psi} d\mathrm{R}. \tag{3.1}$$

The derivatives of the variational energy[51] with respective to a free parameter α is the following (see Appendix A).

$$\overline{E}_\alpha = 2 \left\langle \frac{\Psi_\alpha}{\Psi} (E_L - \overline{E}) \right\rangle_{|\Psi|^2} \tag{3.2}$$

where $E_L = \frac{\hat{H}\Psi}{\Psi}$ is called the local energy, $\overline{E}_\alpha = \frac{\partial}{\partial\alpha}\overline{E}$, $\Psi_\alpha = \frac{\partial}{\partial\alpha}\Psi$, and the notation $\langle\bullet\rangle_{|\Psi|^2}$ means Monte Carlo average using the $|\Psi|^2$ distribution i.e.

$$\langle\Phi\rangle_{|\Psi|^2} \equiv \int \frac{|\Psi|^2}{\int |\Psi|^2 d\mathbf{R}} \Phi d\mathbf{R}.$$

where Φ can be a wave function, local energy, derivatives of them, or products of similar fuctions. The Hessian matrix elements are

$$\begin{aligned}\overline{E}_{\alpha\beta} = 2\Bigg[\left\langle\left(\frac{\Psi_{\alpha\beta}}{\Psi} + \frac{\Psi_\alpha\Psi_\beta}{|\Psi|^2}\right)(E_L - \overline{E})\right\rangle_{|\Psi|^2} - \overline{E}_\beta\left\langle\frac{\Psi_\alpha}{\Psi}\right\rangle_{|\Psi|^2} - \overline{E}_\alpha\left\langle\frac{\Psi_\beta}{\Psi}\right\rangle_{|\Psi|^2}\Bigg] \\ + \left\langle\frac{\Psi_\alpha}{\Psi}E_{L,\beta}\right\rangle_{|\Psi|^2} - \left\langle\frac{\Psi_\alpha}{\Psi}\right\rangle_{|\Psi|^2}\langle E_{L,\beta}\rangle_{|\Psi|^2} + \left\langle\frac{\Psi_\beta}{\Psi}E_{L,\alpha}\right\rangle_{|\Psi|^2} - \left\langle\frac{\Psi_\beta}{\Psi}\right\rangle_{|\Psi|^2}\langle E_{L,\alpha}\rangle_{|\Psi|^2}.\end{aligned} \tag{3.3}$$

The derivatives and the Hessian matrix elements of the variance are

$$(\sigma^2)_\alpha = 2\left\langle E_{L,\alpha}(E_L - \overline{E})\right\rangle_{|\Psi|^2} = 2\left\langle(E_{L,\alpha} - \overline{E}_\alpha)(E_L - \overline{E})\right\rangle_{|\Psi|^2} \tag{3.4}$$

and

$$(\sigma^2)_{\alpha\beta} = 2\left\langle(E_{L,\alpha} - \overline{E}_\alpha)(E_{L,\beta} - \overline{E}_\beta)\right\rangle_{|\Psi|^2} \tag{3.5}$$

As we can see from the equations 3.2, 3.3, 3.4 and 3.5, the gradient and the Hessian matrix elements include terms such as derivatives of the wave function and the local energy with respect to free parameters. Specifically, a pattern is dominant which includes $\hat{O}\Psi/\Psi$ where $\hat{O}$ is an operator. Additionally, Ψ includes a product of Slater determinant and Jastrow factors, however we only consider the derivatives of the Slater determinant since the derivatives of the product can be calculated seperately (see Appendix B), and our study contains the analyze of the impact of several orbital coefficient matrices.

3.1. Derivatives of a Slater Determinant

We start with introducing the Jacobi's formula since it is the basis of the all calculations which expresses the derivative of a determinant in the following way.

$$\frac{d}{dx}\text{det}A(x) = \text{det}A(x) \cdot \text{tr}\left(A(x)^{-1} \cdot \frac{d}{dx}A(x)\right)$$

where A is an invertible $N \times N$ matrix which has elements being a function of x.

For single particle operators, there is a simple formalism developed by Flippi et al. to calculate the derivatives of Slater determinants.[64] Let $\hat{O}$ be a single particle operator and A is the Slater matrix. The derivative is

$$\frac{\hat{O}\text{det}A}{\text{det}A} = \text{tr}(A^{-1}B) \text{ where } B_{ij} = \hat{O}A_{ij}. \tag{3.6}$$

The kinetic energy operator is one of the important examples of a single particle operator

$$\hat{O}(\mathbf{r}_i) = -\frac{1}{2}\nabla_i^2 = -\frac{1}{2}\left(\frac{\partial^2}{\partial x_i^2} + \frac{\partial^2}{\partial y_i^2} + \frac{\partial^2}{\partial z_i^2}\right)$$

where i is the electron index. Equation 3.6 holds using $B_{jk} = -\frac{1}{2}\nabla_i^2 A_{jk}$ which eliminates many operations for calculating the second derivative of the determinants.

For the following part, let us introduce a notation for the derivatives $\partial_\alpha \equiv \frac{\partial}{\partial\alpha}$. Additionally, α and β are used to represent the free parameters.

The derivative of a single particle operator, acting on the determinant, with respect to the free parameter α becomes

$$\frac{\partial}{\partial\alpha}\left(\frac{\hat{O}\text{det}A}{\text{det}A}\right) = \text{tr}(A^{-1}\partial_\alpha B) - \text{tr}[A^{-1}(\partial_\alpha A)A^{-1}B] \tag{3.7}$$

in which $\partial_\alpha A^{-1} = -A^{-1}(\partial_\alpha A)A^{-1}$ is used for the second term, and can be proved as

$$\begin{aligned} AA^{-1} &= I \\ \partial_\alpha(AA^{-1}) &= 0 \\ A\partial_\alpha A^{-1} &= -(\partial_\alpha A)A^{-1} \\ \partial_\alpha A^{-1} &= -A^{-1}(\partial_\alpha A)A^{-1}. \end{aligned}$$

For equation 3.7, since $\hat{O}$ is a single particle operator, only a row or a column survives from the operation in matrix B depending on the implementation. Therefore, the trace of the matrix products can be calculated without effort by using the cyclic property of trace so that only a row or a column becomes non-zero for the resulting matrix. Thus, the trace is equivalent to calculate a single element, which is in the diagonal, from the non-zero row or column.

Using Jacobi's formula, the parameter derivatives of the Slater determinant are

$$\frac{\partial_\alpha \mathrm{det}A}{\mathrm{det}A} = \partial_\alpha \mathrm{ln}(\mathrm{det}A) = \mathrm{tr}(A^{-1}\partial_\alpha A) \tag{3.8}$$

$$\frac{\partial}{\partial\beta}\left(\frac{\partial_\alpha \mathrm{det}A}{\mathrm{det}A}\right) = \partial_\beta\partial_\alpha \mathrm{ln}(\mathrm{det}A) = \mathrm{tr}(A^{-1}\partial_\beta\partial_\alpha A) - \mathrm{tr}[A^{-1}(\partial_\beta A)A^{-1}\partial_\alpha A]. \tag{3.9}$$

Note that in VMC and DMC context, the trial wave function can be represented as an exponential of logaritmic determinants and Jastrow factors in order to ease the calculation. Thus, it is common to come across the term $\partial_\alpha \mathrm{ln}(\mathrm{det}A) = \partial_\alpha \mathrm{det}A/\mathrm{det}A$ (see Appendix B for more details).

3.2. Derivatives of the Trial Wave Function

Equations 3.6, 3.7, 3.8 and 3.9 are the basic equations that are used to calculate the derivatives of the Slater determinants. However, the trial wave function is composed

of a product of two Slater determinants (for up and down electrons). Furthermore, more generally, it is formed by a linear combination of Slater determinant products (note that Jastrow factor is dropped for this chapter).

In the simplest form, the trial wave function is represented as

$$\Psi = \sum_i c_i D_i^{\uparrow} D_i^{\downarrow} \text{ where } D_i^{\sigma} = \det A_i^{\sigma},$$

c_i are the coefficients of the linear combination and σ is the spin of the electrons. The corresponding derivative with respect to an operator $\hat{O}$ is

$$\frac{\hat{O}\Psi}{\Psi} = \frac{1}{\Psi} \sum_i c_i \left[(\hat{O} D_i^{\uparrow}) D_i^{\downarrow} + D_i^{\uparrow} (\hat{O} D_i^{\downarrow}) \right]$$

We can rearrange the equation in order to obtain similar forms for the sake of differentiation.

$$\frac{\hat{O}\Psi}{\Psi} = \frac{1}{\Psi} \sum_i c_i D_i^{\uparrow} D_i^{\downarrow} \left(\frac{\hat{O} D_i^{\uparrow}}{D_i^{\uparrow}} + \frac{\hat{O} D_i^{\downarrow}}{D_i^{\downarrow}} \right) \tag{3.10}$$

With the form of equation 3.10, we can use the equations derived in section 3.1.

There are special cases for $\nabla_{j,\sigma}$ and $\nabla_{j,\sigma}^2$ operators since they only act on the electron j with spin σ. Therefore, opposite spin terms drop from the equation 3.10 as the following.

$$\frac{\nabla_{j,\sigma}\Psi}{\Psi} = \frac{1}{\Psi} \sum_i c_i \left[(\nabla_{j,\sigma} D_i^{\sigma}) D_i^{-\sigma} + D_i^{\sigma} (\nabla_{j,\sigma} D_i^{-\sigma}) \right] \tag{3.11}$$

$$= \frac{1}{\Psi} \sum_i c_i D_i^{\sigma} D_i^{-\sigma} \left(\frac{\nabla_{j,\sigma} D_i^{\sigma}}{D_i^{\sigma}} \right) \tag{3.12}$$

For $\nabla^2_{j,\sigma}$, starting from equation 3.11 and dropping the $-\sigma$ term, the derivative becomes

$$\begin{aligned}\frac{\nabla^2_{j,\sigma}\Psi}{\Psi} &= \frac{1}{\Psi}\sum_i c_i \left[(\nabla^2_{j,\sigma}D_i^\sigma)D_i^{-\sigma} + (\nabla_{j,\sigma}D_i^\sigma)(\nabla_{j,\sigma}D_i^{-\sigma})\right] \\ &= \frac{1}{\Psi}\sum_i c_i D_i^\sigma D_i^{-\sigma}\left(\frac{\nabla^2_{j,\sigma}D_i^\sigma}{D_i^\sigma}\right). \end{aligned} \tag{3.13}$$

The parameter derivatives of $\nabla_{j,\sigma}\Psi/\Psi$ and $\nabla^2_{j,\sigma}\Psi/\Psi$ are the following.

$$\frac{\partial_\alpha \nabla_{j,\sigma}\Psi}{\Psi} = \frac{1}{\Psi}\sum_i c_i D_i^\sigma D_i^{-\sigma}\left[\frac{\partial}{\partial_\alpha}\left(\frac{\nabla_{j,\sigma}D_i^\sigma}{D_i^\sigma}\right) + \frac{\nabla_{j,\sigma}D_i^\sigma}{D_i^\sigma}\left(\frac{\partial_\alpha D_i^\sigma}{D_i^\sigma} + \frac{\partial_\alpha D_i^{-\sigma}}{D_i^{-\sigma}}\right)\right] \tag{3.14}$$

$$\frac{\partial_\alpha \nabla^2_{j,\sigma}\Psi}{\Psi} = \frac{1}{\Psi}\sum_i c_i D_i^\sigma D_i^{-\sigma}\left[\frac{\partial}{\partial_\alpha}\left(\frac{\nabla^2_{j,\sigma}D_i^\sigma}{D_i^\sigma}\right) + \frac{\nabla^2_{j,\sigma}D_i^\sigma}{D_i^\sigma}\left(\frac{\partial_\alpha D_i^\sigma}{D_i^\sigma} + \frac{\partial_\alpha D_i^{-\sigma}}{D_i^{-\sigma}}\right)\right] \tag{3.15}$$

The parameter derivates of the wave function can be calculated using equation 3.10, as well.

$$\frac{\partial_\alpha \Psi}{\Psi} = \frac{1}{\Psi}\sum_i c_i D_i^\uparrow D_i^\downarrow\left(\frac{\partial_\alpha D_i^\uparrow}{D_i^\uparrow} + \frac{\partial_\alpha D_i^\downarrow}{D_i^\downarrow}\right) \tag{3.16}$$

$$\begin{aligned}\frac{\partial_\beta\partial_\alpha \Psi}{\Psi} = \frac{1}{\Psi}\sum_i c_i D_i^\uparrow D_i^\downarrow \Bigg[&\frac{\partial}{\partial_\beta}\left(\frac{\partial_\alpha D_i^\uparrow}{D_i^\uparrow}\right) + \frac{\partial}{\partial_\beta}\left(\frac{\partial_\alpha D_i^\downarrow}{D_i^\downarrow}\right) \\ &+ \left(\frac{\partial_\beta D_i^\uparrow}{D_i^\uparrow} + \frac{\partial_\beta D_i^\downarrow}{D_i^\downarrow}\right)\left(\frac{\partial_\alpha D_i^\uparrow}{D_i^\uparrow} + \frac{\partial_\alpha D_i^\downarrow}{D_i^\downarrow}\right)\Bigg]\end{aligned} \tag{3.17}$$

3.3. Optimization Tests

We perform VMC optimization tests using the new implementation on several quantum dot systems. These tests generally question the reliability of the new algorithm. In the tests, there are several combinations of free parameter optimization procedures; width of the Gaussian basis functions along with the Jastrow factors, first Jastrow factors than the widths, first widths than the Jastrow factors, and optimization of all basis function parameters (positions and widths). The lowest energy is generally obtained from width + Jastrow optimizations, however optimization of all basis function parameters along with the Jastrow factors gives also promising results.

In this section, we present 3 benchmark systems in which widths of the Gaussian basis functions are constrained to be the same in optimization procedures (i.e. only a single width is optimized). Jastrow factors are also optimized simultaneously. The systems are artificial benzene (6 electrons, 3 up and 3 down), triangular AG flake with zigzag edges (13 electrons, 7 up, 6 down) and hexagonal AG flake with armchair edges (42 electrons, 21 up, 21 down). System parameters are $s = 1.4$ and $k = 0$. Several dot radius ρ values are considered in order not to miss any potential problems. Gaussian and TB orbitals are used, starting from different Gaussian width values in order to observe the convergence. Lastly, a comparison of old and new implementation is presented. All values are in atomic units in this section.

Figures 3.1 and 3.2 shows total energy and gaussian width results plotted against optimization iteration for benzene system. A very large number of iterations is choosen to obtain the convergence for the first tests. As shown in Fig. 3.1, except for a single starting Gaussian width value in the lowest dot radius $\rho = 1.27633$ (12.5 nm), energy values converge in 10-15 optimization steps. Regardless of starting width value, Gauss and TB orbitals converge to their respective energy indicating that the implementation is working flawlessly. In Fig. 3.2, the Gaussian width values are shown. Similar to energy, they also converge to respective values for Gauss and TB orbitals yet in larger number of iterations. The convergence occurs in 15-30 steps as ρ increases. Slower convergence behavior indicates that after a critical value, changes in Gaussian widths does not change the energy dramatically. However, it is better to observe the convergence in Gaussian widths since they are the free parameters that alter the nodal structure of the trial wave

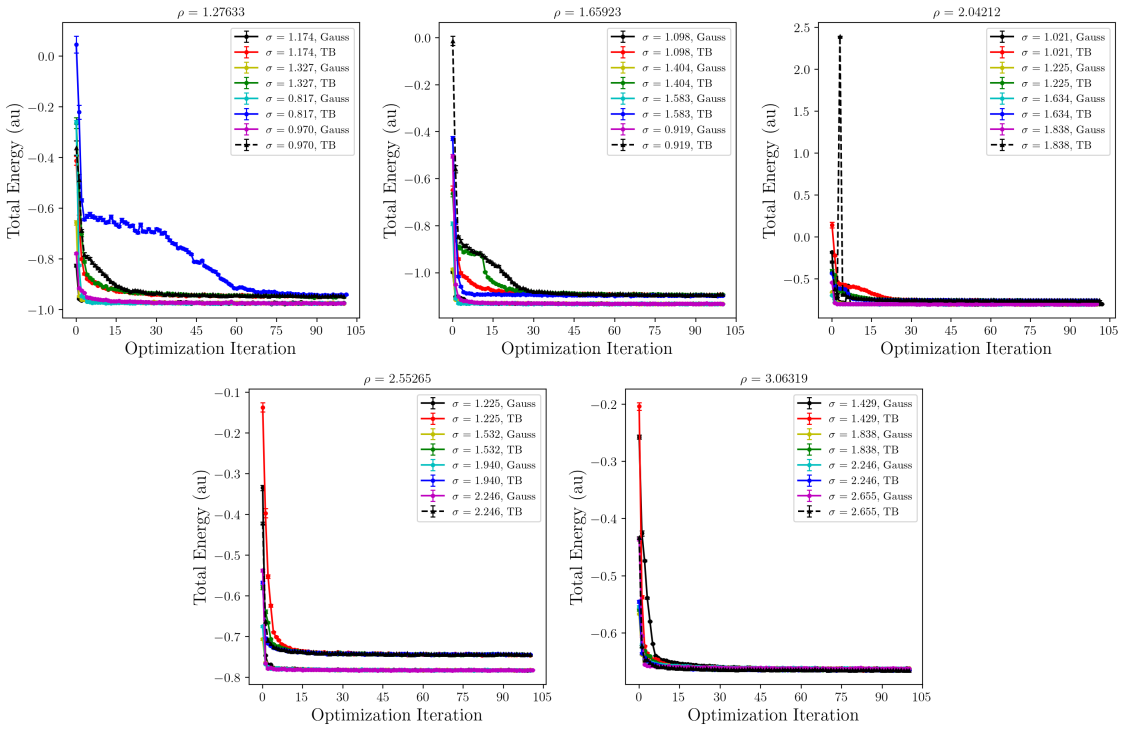

Figure 3.1. Total energy of artificial benzene (3 up, 3 down electrons, $s = 1.4,\ k = 0$) plotted against optimization iteration for several dot radius ρ values. The legends indicate the starting width of the Gaussian basis functions and the orbital type used. All values are in atomic units.

function.

In figures 3.3 and 3.4, the optimization results for triangular AG flake with zigzag edges are shown. There are 13 electrons, 7 up and 6 down. A similar yet better picture is observed for the larger system. The total energies seem to converge around 5-12 optimization steps as seen in Fig. 3.3. In Fig. 3.4, basis function widths converge around 20 steps however they converge faster ($\sim$ 5-10 steps) if they start from good initial values (an educated guess plays somewhat important role here).

The optimization results for the last benchmark system, an hexagonal AG flake with armchair edges (42 electrons, 21 up, 21 down), are shown in Fig. 3.5 and 3.6. The convergence in energy is approximately 10 optimization steps which is a desired property for the largest benchmark system since the computation time increases as the system size increases. Although the basis function widths start from two distinct values, the energies converge smoothly to the same values for Gauss and TB orbitals respectively as seen Fig.

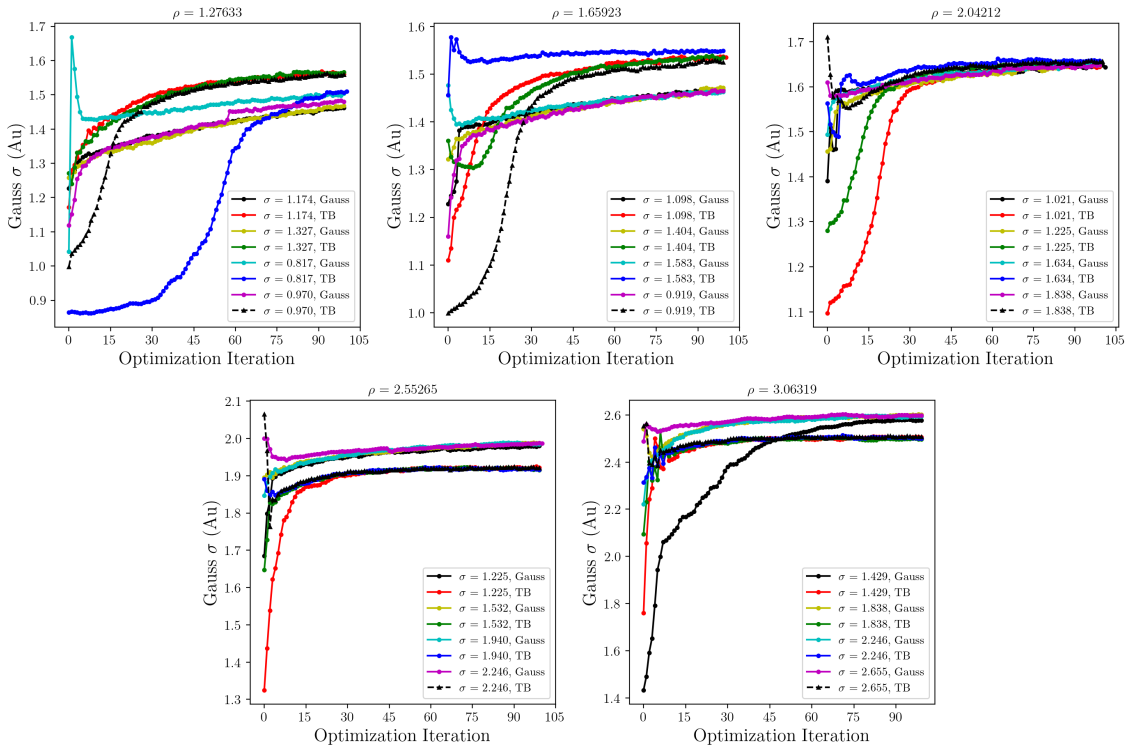

Figure 3.2. Artificial benzene (3 up, 3 down electrons, $s = 1.4,\ k = 0$). Gaussian basis function widths plotted against optimization iteration for several dot radius ρ values. The legends indicate the starting width of the Gaussian basis functions and the orbital type used. All values are in atomic units.

3.5. The convergence of basis function widths is faster for Gauss orbitals yet TB orbitals behave similarly as ρ increases as shown in Fig. 3.6. Despite the number of total iteration being the lowest among benchmark systems, the convergence is the smoothest for basis function widths which is useful for our study since the smallest hexagonal AG flake with armchair edges has 42 sites.

In order to emphasize the requirement of the new algorithm, and to observe the improvement of it, we compare old and new algorithms using from the same input files (the seeds for the random number generator are the same, as well). Both gaussian widths and Jastrow factors are optimized at the same time. In Fig. 3.7, the two columns on the left show a comparison of total energies plotted against optimization iterations. The system contains 42 sites, 42 electrons (21 up and 21 down), and $s = 1.4,\ k = 0$. Several orbital coefficients are used. The calculations are performed on 8 cores per run, using a small number of Monte Carlo steps and optimization steps to save computation time. As

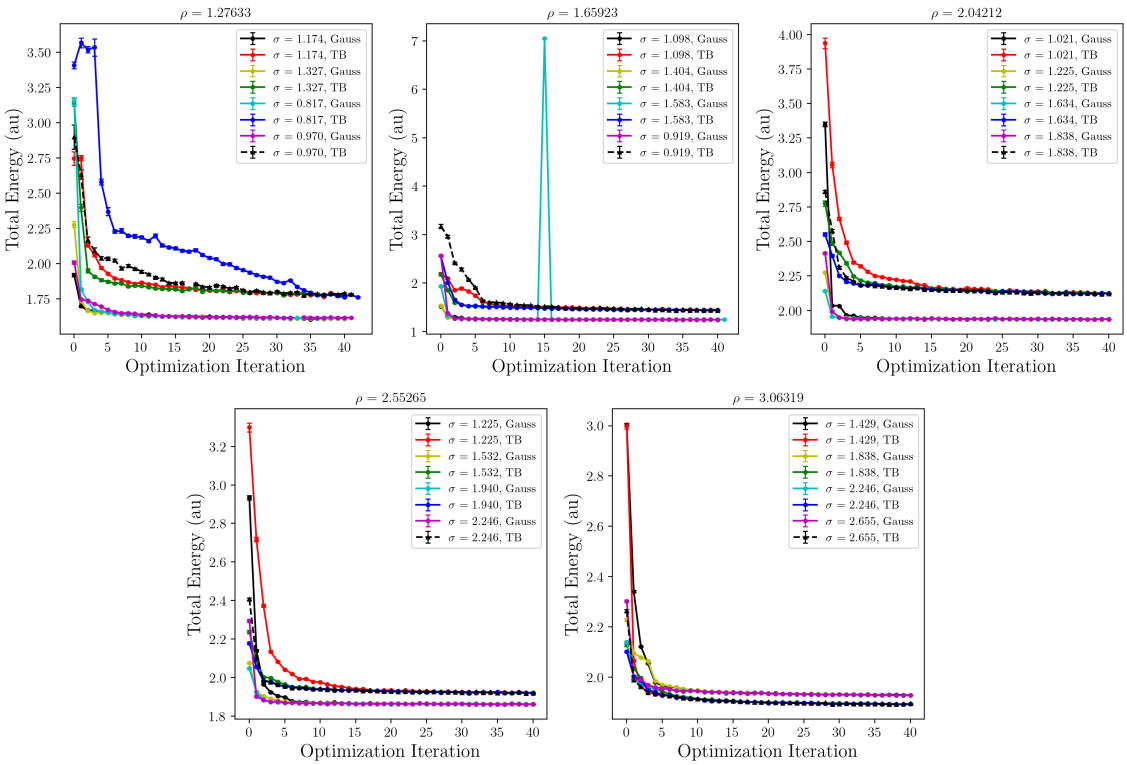

Figure 3.3. Total energy of triangular AG flake with zigzag edges (13 electrons, 7 up, 6 down, $s = 1.4,\ k = 0$) plotted against optimization iteration for several dot radius ρ values. The legends indicate the starting width of the Gaussian basis functions and the orbital type used. All values are in atomic units.

shown in the figure, generally, TB, MFH $U = t$ and $U = 2t$ trial wave functions cannot be optimized and the energy fluctuates around a value using the old algorithm. The fluctuation is more dominant for smaller ρ values, indicating the disability of the liquid-like orbitals to represent more localized states for VMC. Although, the fluctation still present in the new algorithm for the smallest ρ value, it still results in lower energies. As ρ increases, the energy values decrease more smoothly with respect to optimization iteration. A clear distinction is seen for the energies obtained from old and new algorithms. The new implementation obtains lower energies and has smoother decrement in energies with respect to optimization steps. Moreover, in Fig. 3.7, the two columns on the right show a comparison of Gaussian basis function widths. While the old algorithm struggles to get a converge in Gaussian widths and has more fluctuations for the lower ρ values, in new implementation Gaussian widths shows a convergence even in small number of optimization steps.

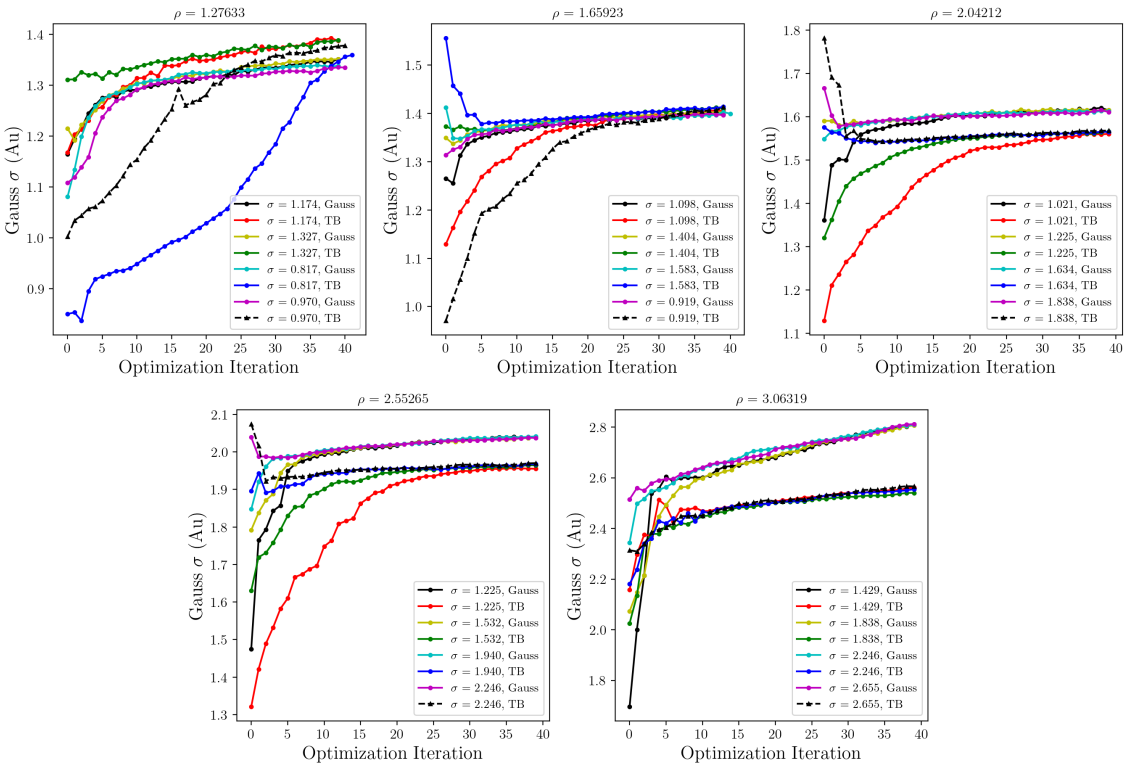

Figure 3.4. Triangular AG flake with zigzag edges (13 electrons, 7 up, 6 down, $s = 1.4$, $k = 0$). Gaussian basis function widths plotted against optimization iteration for several dot radius ρ values. The legends indicate the starting width of the Gaussian basis functions and the orbital type used. All values are in atomic units.

Implementation of the new algorithm is an improvement to the existing procedure that it does not only allows us to perform calculations using non-diagonal orbital coefficients but also improves the convergences, and lowers the overall computation time.

3.4. Summary

In summary, a new implementation is applied in order to calculate the derivatives of the desired quantities (energy, variance, trial wave function) with respect to tunable parameters when the orbitals in Slater determinants are a linear combination of localized Gaussian functions. In this case, the coefficient matrix has non-zero values in non-diagonal elements which makes it impossible to use Sherman-Morrison formula. We calculate the derivatives using a method developed by Filippi et al.[64] The new implemen-

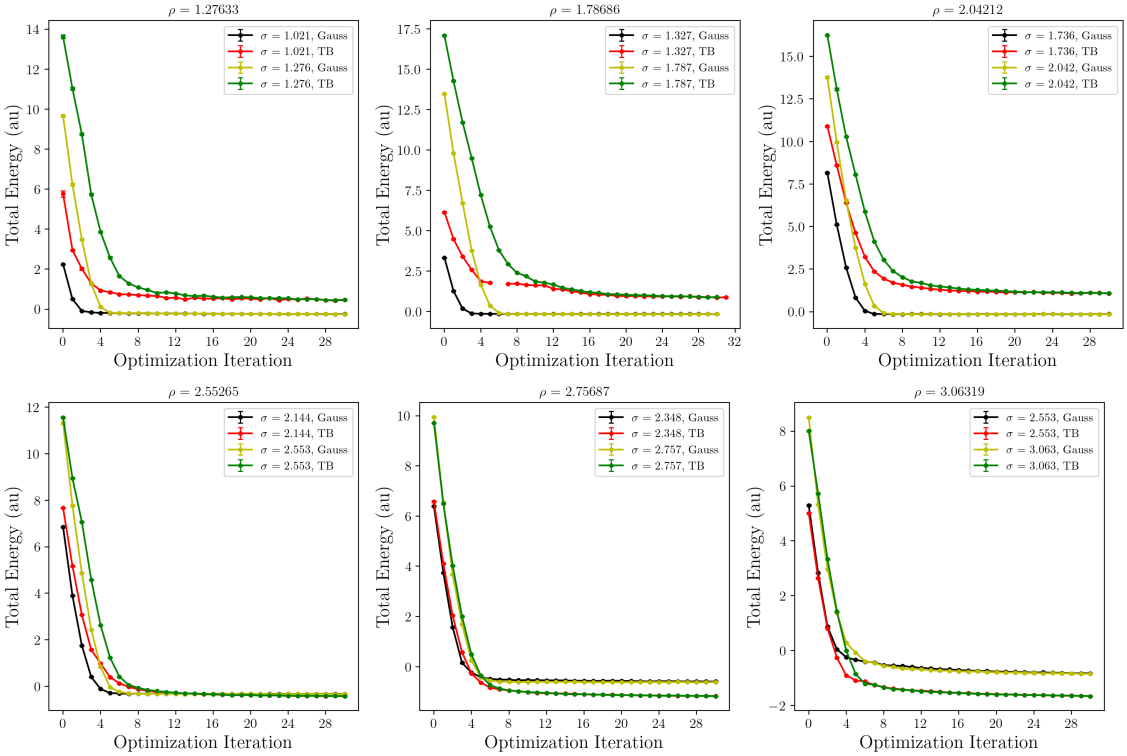

Figure 3.5. Total energy of hexagonal AG flake with armchair edges (42 electrons, 21 up, 21 down, $s = 1.4,\ k = 0$) plotted against optimization iteration for several dot radius ρ values. The legends indicate the starting width of the Gaussian basis functions and the orbital type used. All values are in atomic units.

tation enables the algorithm to work with various orbital coefficient matrices and improves its convergence speed.

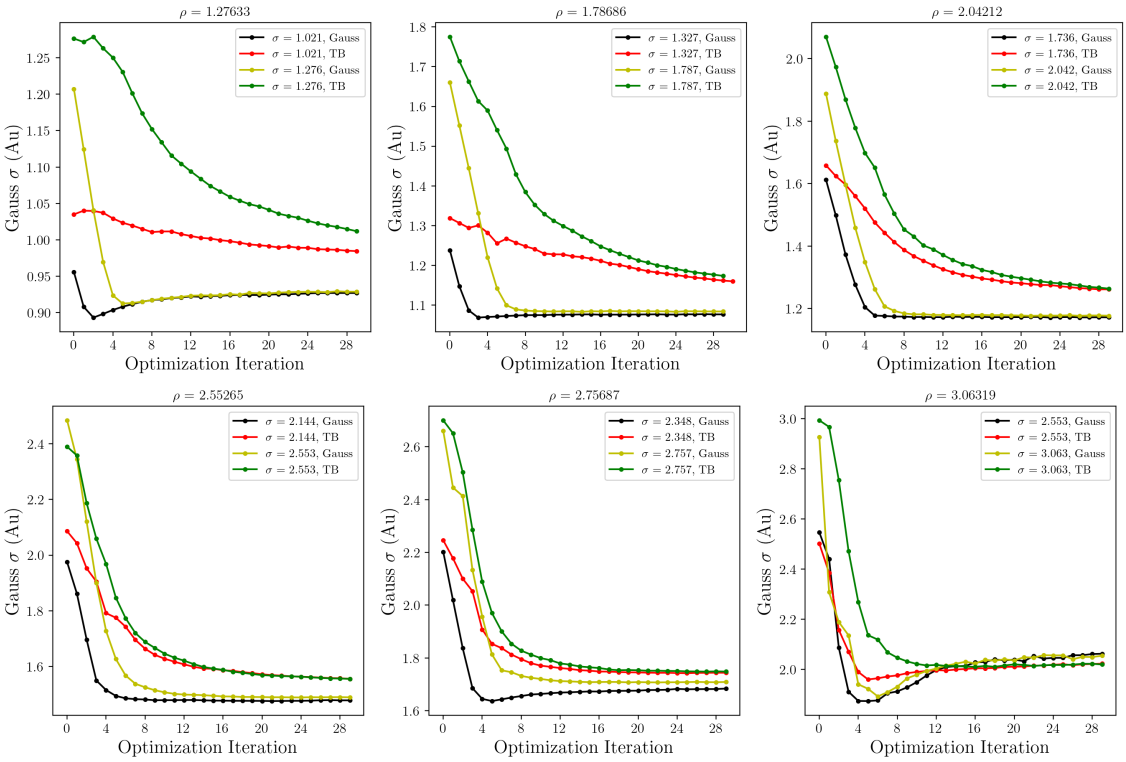

Figure 3.6. Hexagonal AG flake with armchair edges (42 electrons, 21 up, 21 down, $s = 1.4$, $k = 0$). Gaussian basis function widths plotted against optimization iteration for several dot radius ρ values. The legends indicate the starting width of the Gaussian basis functions and the orbital type used. All values are in atomic units.

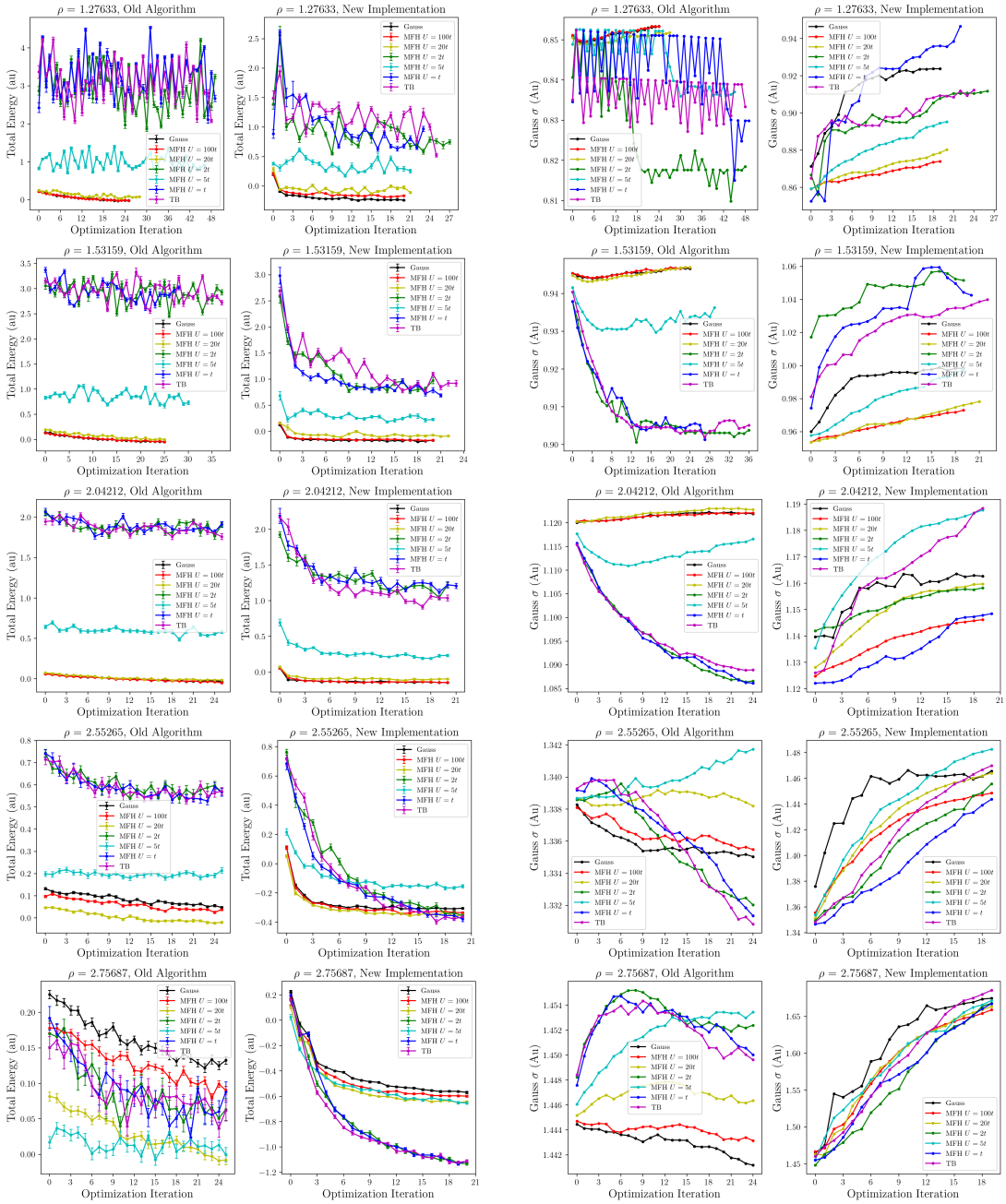

Figure 3.7. Hexagonal AG flake with armchair edges (42 electrons, 21 up, 21 down, $s = 1.4$, $k = 0$). Optimization comparison of old and new algorithms. Energies (two columns on the left) and Gaussian basis function widths (two columns on right) plotted against optimization iteration for several orbital coefficients and radius ρ values. All values are in atomic units.

CHAPTER 4

TIGHT-BINDING AND MEAN-FIELD HUBBARD HAMILTONIAN DIAGONALIZATION RESULTS

In this chapter, we present TB and MFH calculations in order to construct a basic insight about trial wave functions and AG systems. The obtained eigenvectors are used to construct orbitals in Slater determinants, as linear combination coefficients, as described in Section 2.3. The analysis of these results also provide information about the state of the system depending on the type of orbitals used in trial wave function.

We work on two flake geometries[33] that our inspiration is originated from TB and MFH calculations of real graphene. They are a hexagonal flake with armchair edges (42 electrons and quantum dots), and a triangular flake with zigzag edges (46 electrons and quantum dots). MFH predictions state that while density of states of armchair hexagon flake closely similar to bulk graphene with a small band gap, zigzag triangular flake have available energy levels inside the band gap contributed from edge states which are completely spin polarized due to the broken spin symmetry of triangular zigzag geometry.[33,65,66]

However, this thesis only covers the hexagonal flake geometry with armchair edges. The systems are prepared according to Lieb's theorem[67]; there are 21 up and down electrons for the armchair hexagonal flake.

Diagonalization of TB Hamiltonian for 42 quantum dots and 42 electrons shows that armchair hexagonal flake of AG exhibits a small gap opening near Fermi level (similar to real graphene quantum dots) about 1 units in terms of t as seen in Fig. 4.1a. For real graphene, a band gap can be introduced by just forming a finite sized flake, and may be even controlled using different flake and edge geometries (from which some of the fabrication and reliability issues are originated). However, in AG systems, this band gap can easily be controlled by changing the hopping parameter t which is related to several tunable parameters of AG: the radius of the confinement potentials (affects the overlap between the potentials) and the lattice constant a.

TB calculations show a uniform electron density distributed among lattice sites as

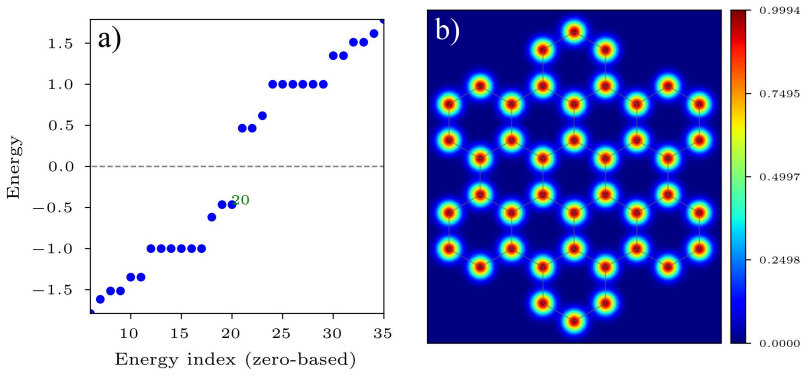

Figure 4.1. Exact diagonalization results for tight-binding Hamiltonian. Armchair hexagonal flake with 42 electrons and quantum dots. a) Tight-binding energy spectra. Energy values in the y-axis are in terms of hopping parameter t. b) Total electron densities are not normalized, and calculated using gaussian kernel with radius $\sigma = 0.2a$, where a is the lattice constant.

in Fig. 4.1b. There is no spin information which can be extracted from TB calculations since the total spin of the system is $S_z = 0$ (number of up and down electrons is equal), and the Hamiltonian is spin symmetrical. If S_z was not equal to zero, up and down electron occupancies of the states would not be equal and we would get a spin structure even though the Hamiltonians of the up and down electrons are equal (since up and down electron densities would differ).

Self-consistent MFH calculations reveal two different phases depending on the ratio U/t, yet the electron densities are exactly the same as TB calculations (Fig. 4.1b). For $U/t = 2$, MFH calculations show a metallic-like phase similar to TB results. Fig. 4.2a shows similar energy spectra even though the spin symmetry is broken for MFH Hamiltonian. In Fig. 4.2b, spin densities for MFH $U/t = 2$ calculations seem to have an AFM ordering which is diminishing towards the center, however the polarizations are in the order 10^{-6} indicating no spin structure as in TB results. MFH $U/t = 20$ calculations shows a wider band gap in Fig. 4.2c. As U increases, electron-electron interactions dominate the kinetic energy of the electrons (which is related to hopping parameter t), and strong localizations occur at the lattice sites, which results in an insulator phase. Fig. 4.2d shows that there is clearly an AFM ordering for MFH $U/t = 20$ calculations, strong spin polarizations occur at the lattice sites.

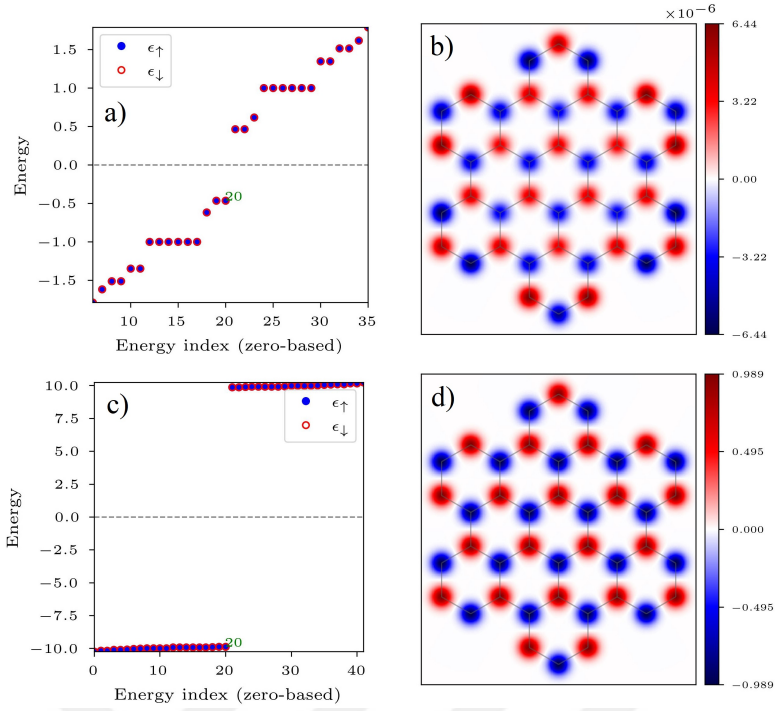

Figure 4.2. Self-consistent mean-field Hubbard calculations. Armchair hexagonal flake with 42 electrons and quantum dots. a) Mean-field Hubbard energy spectra for $U/t = 2$. b) Spin densities for $U/t = 2$. c) Mean-field Hubbard energy spectra for $U/t = 20$. d) Spin densities for $U/t = 20$. Energy values in the y-axis are in terms of hopping parameter t. Spin densities are not normalized, and calculated using gaussian kernel with radius $\sigma = 0.2a$, where a is the lattice constant.

4.1. Summary

In conclusion, we perform calculations using TB and MFH Hamiltonians. The eigenvectors obtained from diagonalization of TB and MFH Hamiltonians are used in formation of trial wave functions for QMC calculations in the next chapter. The exact diagonalization results show that the trial wave functions prepared using TB and MFH $U/t = 2$ orbitals can represent liquid phases in which electrons are free to move with almost non-existent spin correlations. On the other hand, the trial wave functions prepared using MFH $U/t = 20$ orbitals can represent more localized phases with strong electron correlations and broken spin symmetry.

CHAPTER 5

METALLIC TO ANTIFERROMAGNETIC TRANSITION RESULTS

In this chapter, we present results for metallic to antiferromagnetic phase transition in AG flakes with hexagonal armchair geometry. We prepare three types of orbitals in Slater determinants of trial wave functions, as mentioned in Chapters 2 and 4. The free parameters in trial wave functions are optimized using VMC, and ground states is projected out by DMC method within fixed node approximation. We analyze the systems depending on quantum well radius ρ at difference quantum well sharpness values s. For each ρ value, we compare the DMC energies between the results from different trial wave functions. The state with the minimum energy is selected as the ground state of the system at a given ρ value. We analyze the spin densities of the systems to explain a possible phase transition. We perform calculations with 2 different system sizes as 42 and 114 sites. Lastly, we implement a new basis function in order to obtain better representation of the ground states of the system.

In the beginning of our calculations, potential depth V_0 values are tuned for each sharpness s and dot radius ρ values. For too high values of V_0, confinement potential strength may not be enough to keep electrons near the sites, and electrons tend to escape the system. For too low values of V_0 over localization occurs. Our first aim is to keep the electrons in the system, and adjusting the VMC total energies close to 0 meV since we try to mimic the charge neutral behavior of graphene. Divergence of total energy away from 0 can be interpreted as in two cases: the system would borrow electrons from surroundings (which breaks charge neutrality), or there would be more than one states in the quantum wells (in which the density uniformity is broken). Adjusting VMC energies around 0 reveals an approximately linear behavior for V_0 values with respect to dot radius ρ for all sharpness s values, shown in Fig. 5.1.

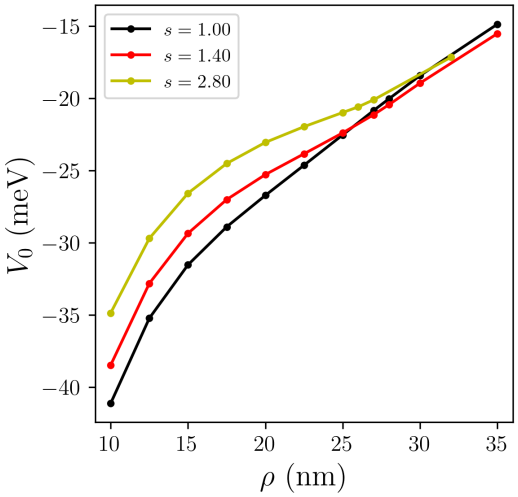

Figure 5.1. V_0 values to keep the system charge-neutral depending on dot radius, using different potential sharpness values, obtained from VMC calculations.

5.1. Density Functional Theory Stability Analysis

Suitability of selected V_0 values should be examined since Dirac cone structure of 2D bulk AG system should not be broken while keeping the AG flake charge neutral with selected parameters. Therefore, DFT calculations of bulk AG have been performed within the local density approximation.[33] The Dirac cone structure is preserved for the range $\rho = [12.5, 30]$ nm, as shown in Fig. 5.2a-b for ρ = 15 - 25 nm. Outside this range the Dirac fermion picture becomes distorted. Additionally, using DFT and single particle solutions of Schrödinger equation, hopping parameter t and Hubbard U are predicted as mentioned in section 2.3. In the inset of Fig. 5.2, we plot U/t with respect to ρ which shows a fast decay from ≈300 to 50 between ρ = 15 and 20 nm. These results indicate that the critical U/t value for a metal-insulator transition in AG is much higher than the critical value of ∼3.8 predicted by Hubbard calculations[21–24], presumably due to the importance of long-range interactions and deviation from the nearest-neighbor TB approximation as ρ increases. Although the general trend of U/t vs. ρ provides a basic insight about the underlying mechanics (electrons are more mobile at higher ρ values), trial wave functions prepared using high U/t values ($300 \sim 50$) do not provide the most suitable nodal structures for QMC calculations. In fact, we observed that simplest TB

trial wave functions works best for the whole set of parameters.

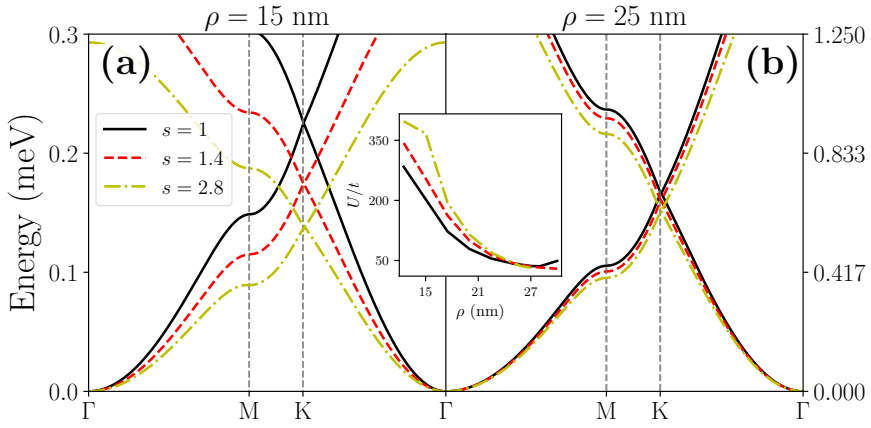

Figure 5.2. DFT band structure calculations of bulk artificial graphene for (a) $\rho = 15$ nm and (b) $\rho = 25$ nm. Inset figure shows that U/t ratio plotted against dot radius ρ, predicted by DFT and single particle calculations.[33]

5.2. Quantum Monte Carlo Results

Our first significant result starts with a cross-over in the VMC energies depending on dot radius ρ as shown in Fig. 5.3a. These results are obtained for armchair hexagonal AG flake with 42 sites and 42 electrons. Quadratic gate potential is turned off ($k = 0$). At low ρ values the minimum energy is represented by gaussian and MFH $U = 20t$ trial wave functions. A cross-over occurs at $\rho \approx 27$, TB and MFH $U = 2t$ orbitals take the lead for higher ρ values. Even analyzing the VMC energies gives a hint that there may be a phase transition from a strongly localized state to a more metallic state depending on dot radius since gaussian and MFH $U = 20t$ orbitals represents localized states while TB and MFH $U = 2t$ describe unconfined states. DMC results, however, reveal a slightly different picture as shown in Fig. 5.3b. From $\rho = 10$ nm to $\rho \approx 18$ nm, all trial wave functions give similar energies within the statistical error bars, and split around $\rho \approx 18$ nm. After the split, the ground state of the system is represented by TB and MFH $U = 2t$ trial wave functions. DMC results support the VMC prediction about the ground state exhibiting a phase transition, yet around another dot radius value. It might also be noted that surprisingly TB trial wave functions have equally good nodal

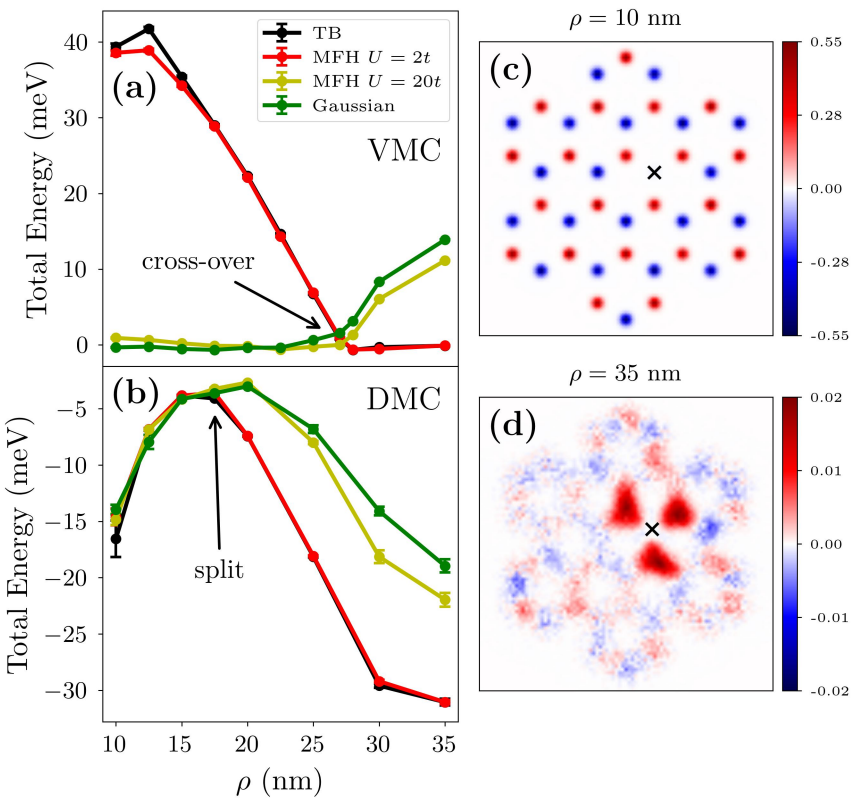

Figure 5.3. Armchair hexagonal flake results, 42 sites, 42 electrons, $s = 1.4$ and $k = 0$ plotted for several trial wave functions.[33] (a) VMC total energy vs ρ. (b) DMC total energy vs ρ. (c) Extrapolated pair spin density results for $\rho = 10$ nm, using tight-binding trial wave function. (d) Extrapolated pair spin density results for $\rho = 35$ nm, using tight-binding trial wave function. The reference electron is located at the X marked point for c and d.

structure as gaussian trial wave functions at lower ρ values. In order to reveal underlying electronic and magnetic structure, we perform pair density calculations. The pair density $p_{\sigma\sigma_0}(\mathbf{r}, \mathbf{r}_0)$ is probability of finding an electron with spin σ at location $\mathbf{r}$ when an electron with spin σ_0 is fixed at location $\mathbf{r}_0$. For underlying magnetic correlations, we calculate pair spin densities $p_{\uparrow\downarrow}(\mathbf{r}, \mathbf{r}_0) - p_{\downarrow\downarrow}(\mathbf{r}, \mathbf{r}_0)$ and $p_{\downarrow\uparrow}(\mathbf{r}, \mathbf{r}_0) - p_{\uparrow\uparrow}(\mathbf{r}, \mathbf{r}_0)$. This can reveal complex magnetic behavior of the systems especially when the total spin of the system is $S_z = 0$. In Fig. 5.3c and 5.3d, pair spin density results of ground states are shown for $\rho = 10$ nm and $\rho = 35$ nm respectively for a reference fixed point at the top of a lattice site (X marked point). This lattice site is chosen to break spin symmetry, and it is away from the edges. At $\rho = 10$ nm, electrons are strongly localized and polarized leading to an AFM insulator

phase. All trial wave functions have similar spin densities until $\rho \approx 18$ nm. After 18 nm, spin-spin correlations become weak and short-ranged resulting to a metallic phase at high ρ values as in Fig. 5.3d. Thus, pair spin density calculations also confirm metal - AFM insulator transition prediction, and it is consistent with earlier studies mentioning the phase transition.[25] Additionally, VMC energy cross-over and DMC energy split behaviors of the systems occur (so that the phase transition) in all sharpness s values as shown in Fig. 5.4. For $s = 2.8$, the overlap between the confinement potentials is too high for higher ρ values. The system becomes a single large quantum well with small deviations resulting into unstable QMC results after $\rho \approx 32$ nm.

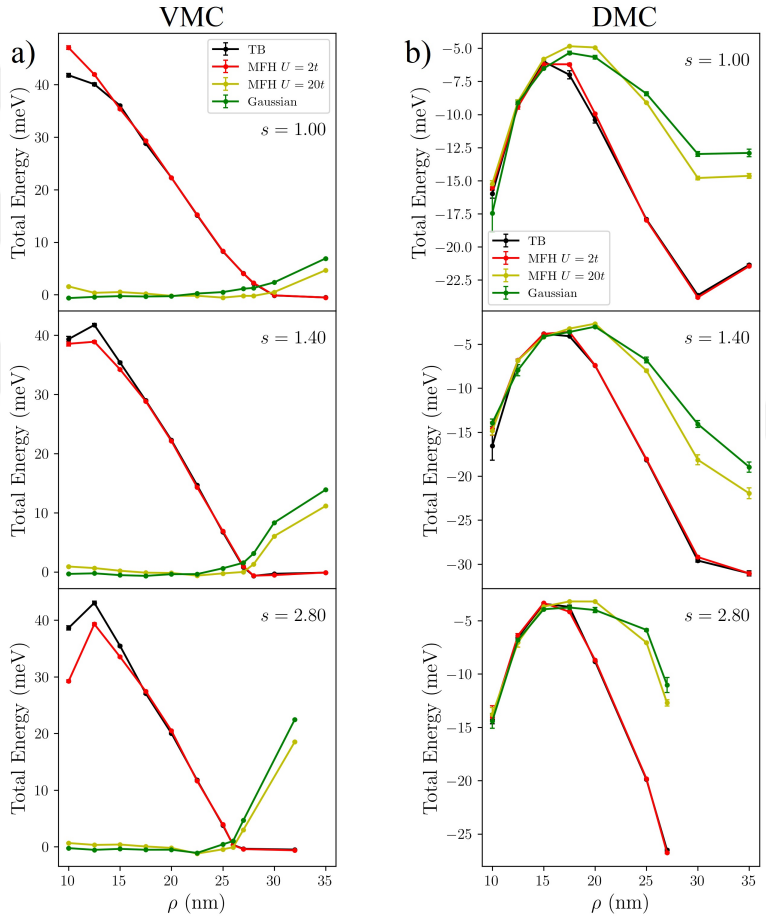

Figure 5.4. Armchair hexagonal flake results, 42 sites, 42 electrons, all s values and $k = 0$ plotted for several trial wave functions.

The charge neutral behavior of real graphene is imitated by tuning V_0 values in the systems discussed so far, however the long-range interactions still affect the charge

distribution which disrupt the charge uniformity due to the finite size of the systems. Such an effect can be seen in Fig. 5.5a-c, the total electron densities for the armchair hexagonal. flake and zigzag triangular flake with $s = 1.4$ and $\rho = 25$ nm ($k = 0$)[33] Coulomb interactions between the electrons push them towards the edges of the hexagonal flake unlike real graphene quantum dots in which the charges are distributed uniformly. In principle, the charge uniformity can be achieved by decreasing V_0 value further, however over localization occurs as we mentioned before, and the system would be negatively charged. In order to overcome finite size effects, we apply a quadratic gate potential to the system controlled by the parameter k in equation 1.1. When $k \neq 0$, quadratic gate potential attracts the electrons towards the center of the system so that the charge uniformity is preserved, and finite size effects are minimized as shown in Fig. 5.5b for $k = 3.56 \times 10^{-4}$ meV/nm^2.

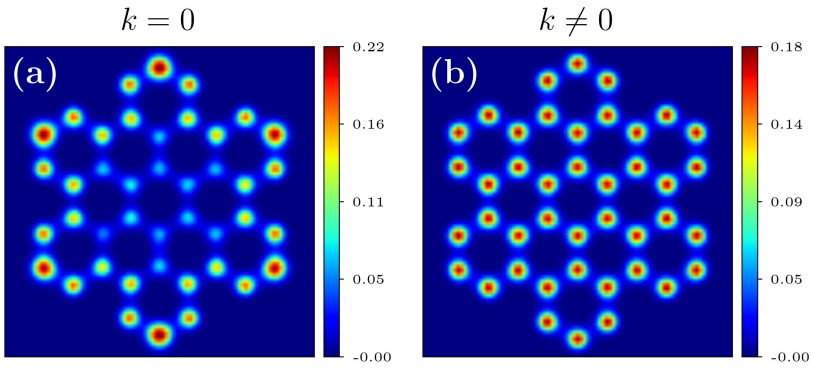

Figure 5.5. Effect of k on total electron densities for armchair hexagonal flake. $s = 1.4$ and $\rho = 25$ nm, using tight-binding trial wave function.[33] (a) $k = 0$. (b) $k = 3.56 \times 10^{-4}$ meV/nm^2.

In order to validate our predictions on AG quantum dots using charge non-uniform systems ($k = 0$), all calculations are repeated by choosing appropriate k values that restores the charge uniformity of the systems for all s values. Since electrons are uniformly localized inside the quantum wells for $k \neq 0$, quadratic gate potential adds approximately a constant value to the total energy. Thus, the total energy can be shifted by this value to examine charge neutrality behavior. In Fig. 5.6, a comparison is shown for VMC and DMC energies when $k \neq 0$ using all s and ρ values. When the energies are shifted, the DMC energies are still close to 0 meV as shown in Fig. 5.6b, which ensures the charge

neutrality. A cross-over in VMC energies and split in DMC energies also occur as in Fig. 5.3. However, the cross-over in VMC energies is shifted to $\rho \approx 32$ nm, and the split in DMC energies is shifted to $\rho \approx 26$ nm. For $s = 2.8$, the split is present but with a small difference in the energies, and the increasing overlap between the potential wells makes QMC calculations unstable even for the uniform distribution (large ρ values are trivial as we discussed before).

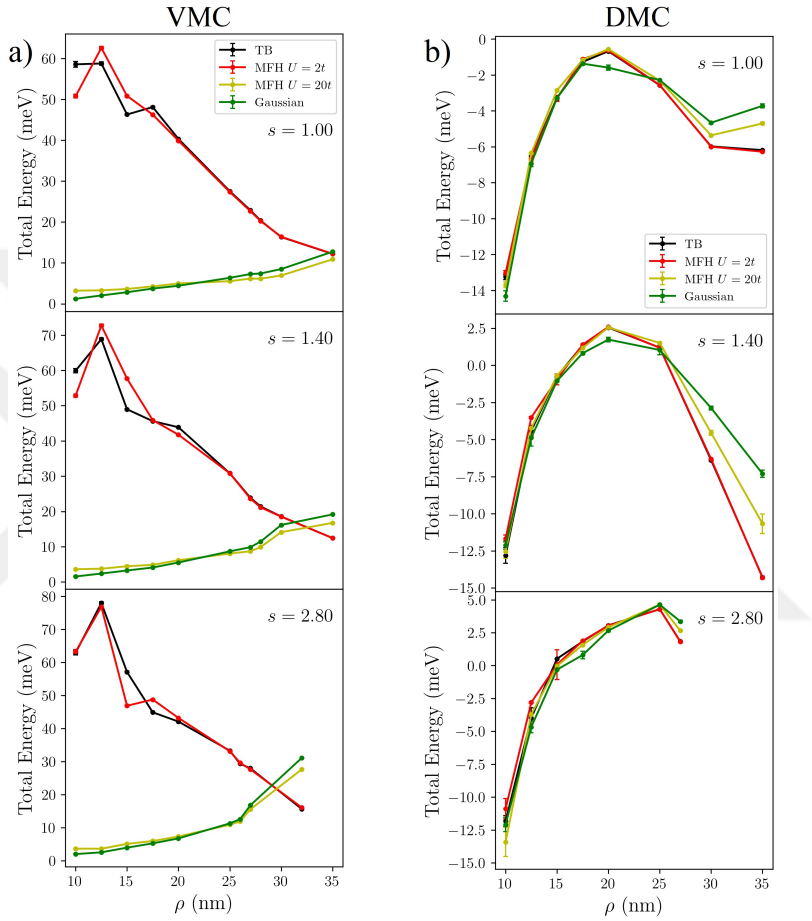

Figure 5.6. Armchair hexagonal flake results, 42 sites, 42 electrons, shifted energy values for all s values and $k \neq 0$ plotted for several trial wave functions.

In order to examine the phase transition in more detail, we calculate a real-space spin-spin correlation function[33], g, normalized by the density-density correlations,

$$g = \frac{\langle s_i s_j \rangle}{\langle n_i n_j \rangle} \tag{5.1}$$

where s_i and n_i are the average total spin and average total electron densities on site i within a radius r, and i, j are the nearest neighbor sites. We use $r = a/2$ in all spin-spin correlation calculations, where a is the lattice constant. $\langle\rangle$ represents an average over nearest neighbor indices, i, j. Normalization ensures that output values of the function

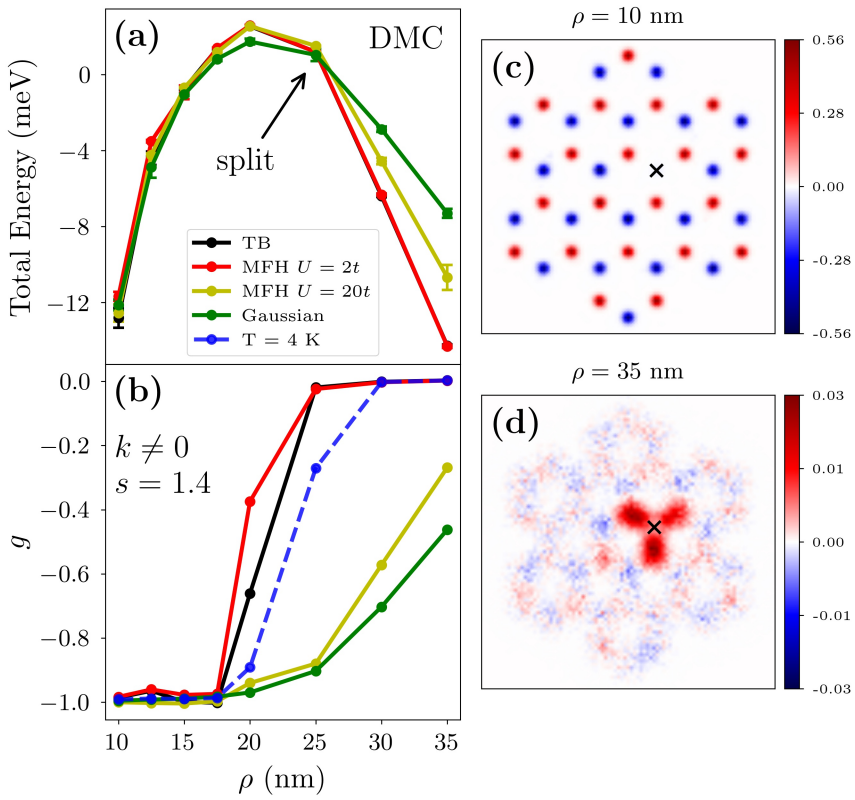

Figure 5.7. Armchair hexagonal flake results, 42 sites, 42 electrons, for $s = 1.4$ and $k = 3.56 \times 10^{-4}$ meV/nm^2. (a) DMC energy results shifted by approximate total gate potential value. (b) Extrapolated spin-spin correlation function. (c) Extrapolated pair spin density results for $\rho = 10$ nm, using tight-binding trial wave function. (d) Extrapolated pair spin density results for $\rho = 35$ nm, using tight-binding trial wave function. The reference electron is located at the X marked point for c and d.

remain in $[-1, 1]$ range, with $g = -1$ corresponding to AFM and $g = 0$ corresponding to metallic configuration ($g = 1$ means that all spins are in the same direction, which does not happen in the subspace $S_z = 0$ considered here). In Fig. 5.7b, g is plotted against ρ for several trial wave functions with $s = 1.4$ and $k = 3.56 \times 10^{-4}$ meV/nm^2 (chosen for charge uniformity). There is also a weighted average of the results of all trial wave functions, using Boltzmann distribution at $T = 4$ K, in order not to miss any effects for

the points that DMC energies are close to each other within statistical noise. The ground state of the system remains strongly AFM between $\rho = 10$ nm and $\rho = 18$ nm as shown in Fig. 5.7b. A smooth transition occurs between $\rho = 18 - 30$ nm. Although it seems sharp for TB and MFH $U = 2t$ trial wave functions, similar energies in that region lead to a smooth transition for the weighted average. After $\rho = 30$ nm, the system exhibits a completely metallic phase. Notice that the transition happens around DMC energy split $\rho \approx 26$ nm as seen in Fig. 5.7a. In Fig. 5.7c and 5.7d, pair spin densities are shown to build an intuition about spin-spin correlation function for both AFM phase at $\rho = 10$ nm and metallic phase at $\rho = 35$ nm.

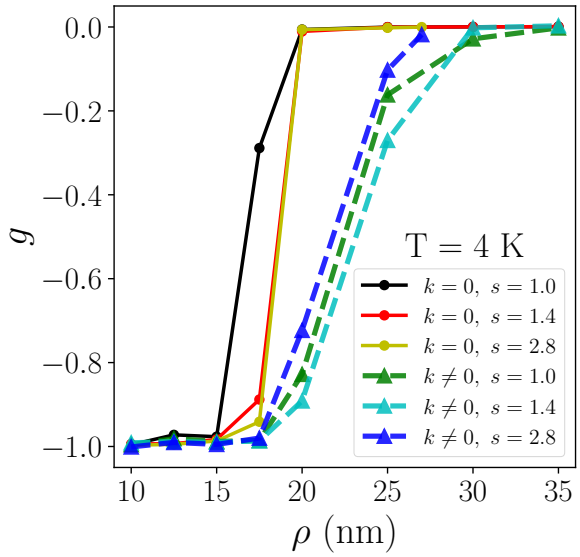

Figure 5.8. Armchair hexagonal flake results, 42 sites, 42 electrons, for weighted averages of all s and k values at 4 K.[33]

In Fig. 5.8, weighted averages from all s and k combinations are summarized.[33] The system undergoes the phase transition for all parameters depending on dot radius. The potential sharpness s does not have a significant effect on the transitions. The AFM insulator to metallic phase transition occurs for both uniform ($k \neq 0$) and nonuniform ($k = 0$) charge distributions, however for the systems having nonuniform charge distribution the transition is sharper and occur in lower ρ values.

5.3. Flake Size Effects

In this section we present results for a large system, an armchair hexagonal flake with 114 sites and 114 electrons. We investigate the stability of the AFM insulator to metallic phase transition under changing system size.

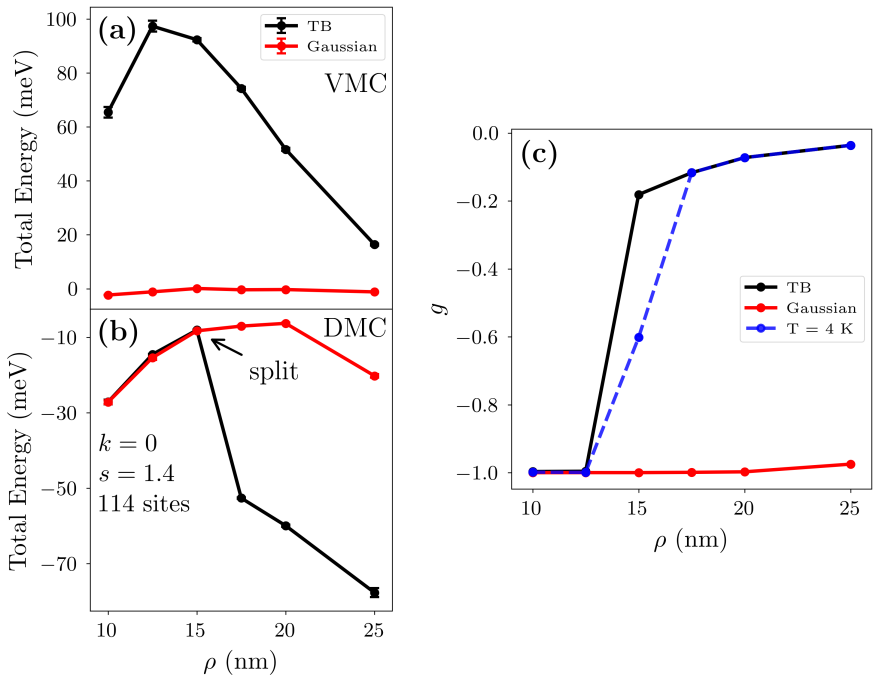

Figure 5.9. Armchair hexagonal flake results, 114 sites, 114 electrons, $s = 1.4$ and $k = 0$ plotted for several trial wave functions. (a) VMC total energy vs ρ. (b) DMC total energy vs ρ. (c) Extrapolated spin-spin correlation function.

Fig. 5.9 shows the first significant results of the large system size. We choose the intermediate sharpness value $s = 1.4$ and $k = 0$ for these calculations. TB and gaussian trial wave functions are used since they represent two ends of the phase transition, a metallic-like behavior (TB) and a localized behavior (gaussian). MFH $U = 2t$ and $U = 20t$ trial wave functions are not used for the sake of saving computation time. Potential depth value V_0 is tuned to set energies close to zero (for charge neutrality). Unlike the small system (Fig. 5.3a), VMC energies do not exhibit a cross-over between two different trial wave function groups as shown in Fig. 5.9a. The minimum energy is represented by the gaussian trial wave function for all ρ values. However, the DMC energies of two

trial wave functions split around $\rho \approx 16$ nm after they give similar enerjies within the statistical error bars as shown in Fig. 5.9b. Similar to the small system, the ground state is represented by TB trial wave function after the split. DMC energies clearly indicates a phase transition from a localized state to a metallic state, which is verified by spin-spin correlation function, in Fig. 5.9c. The weighted average of spin-spin correlation function shows an AFM insulator to metallic phase transition around $\rho \approx 16$ nm.

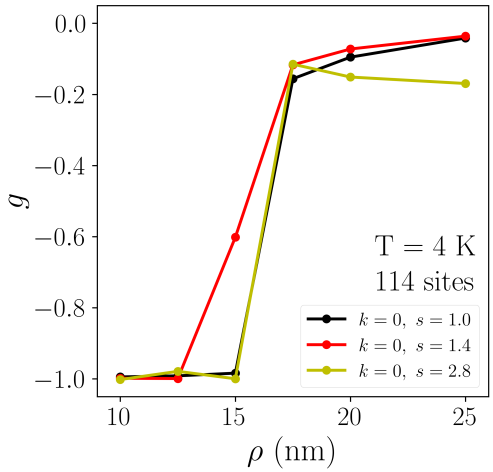

Figure 5.10. Armchair hexagonal flake results, 114 sites, 114 electrons, $k = 0$ for weighted averages of all s values at 4 K.[33]

The phase transition exists for different potential sharpness values on the large system. A summary of weighted averages from all s values is shown in Fig. 5.10. Although the system has nonuniform charge distribution ($k = 0$), the phase transition occurs around $s \approx 16$ nm, and slightly smoother for $s = 1.4$. The results of the large system are consistent with the small system; the only difference is that the phase transition is around a smaller potential radius value on large system.

5.4. Basis Function Comparison

In order to represent the states with a function having more flexible nodal structure, another basis function is tried. The aim is to obtain lower energies and better nodal structure from VMC optimizations, and to expect better results and statistics from DMC

calculations.

The new basis function is so-called “Leaky Gaussian” function which has the following form (see Appendix C for details).

$$\phi(\mathbf{r}) = (1 - \beta|\mathbf{r}|^2)\exp(-\alpha|\mathbf{r}|^2/2) \tag{5.2}$$

where α is the inverse square of the width of the Gaussian part, β is the leak term that $\beta \geq 0$, and $\mathbf{r}$ is the position of the electron. The effect of the leak term β is shown in Fig.

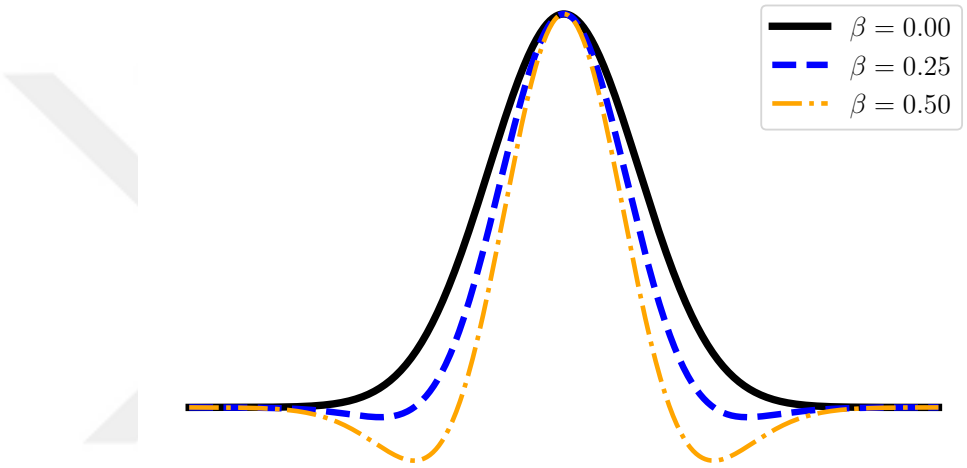

Figure 5.11. Leaky Gaussian basis function, $\alpha = 1$ plotted for several β values.

5.11. It adds nodes to the base Gaussian function and changes the position of the nodes.

A comparison of the original Gaussian basis function and the leaky Gaussian basis function is shown in Fig. 5.12 and 5.13 for $\rho = 15$ nm and $\rho = 25$ nm, respectively. The benchmark system is a triangular flake with zigzag edges containing 13 sites and 13 electrons (7 up, 6 down). The original Gaussian basis function is indicated as “OLD” in the figures, and is taken as the reference line for comparison. In all calculations, Gaussian widths (α) and Jastrow factors are optimized. For the new function, β values are taken as constant and scanned in the range $\beta = [0, 0.2]$. As seen from both figures, the new function has no improvements over the old function for VMC energies. The optimizations performed with the original Gaussian function are better for both TB and Gauss orbitals,

and for all β values for new function. Additionally, for DMC energies, the new function not only results in higher energy values but also has worse statistics as seen from the population control error bars.

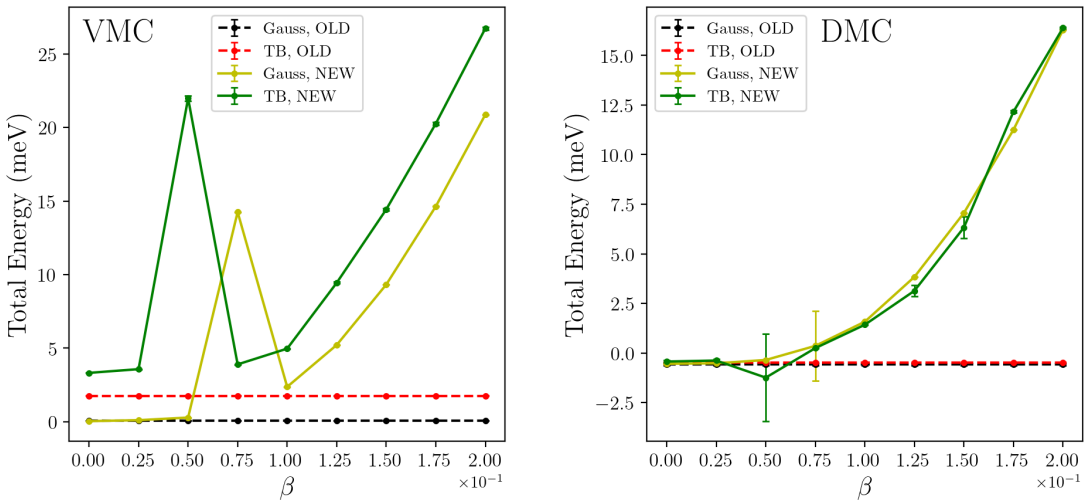

Figure 5.12. Comparison of total energies plotted against leak term β of new gaussian basis function. The result of old basis function used as a reference line. The system is a triangular flake with zigzag edges (13 electrons, 7 up, 6 down), $s = 1.4$, $k = 0$ and $\rho = 15$ nm.

Since the new function cannot perform well even for a simple system, we can conclude that it is not suitable for our systems. Therefore, for quantum dot systems having the hexagonal lattice structure, the original Gaussian function is better for both energy values and statistical behavior of the simulations.

5.5. Summary

In summary, we perform VMC and DMC calculations with several trial wave functions depending on quantum well radius ρ, sharpness s and flake sizes. As we analyze the real space spin-spin correlation function, we conclude that the system exhibits a metallic to AFM phase transition as ρ decreases, and it does not depends on s and flake size. The transition is smoother when we eliminate the finite size effects.

We also perform calculations with a new basis function called leaky Gaussian function which introduces a more flexible nodal structure. However, the observation is

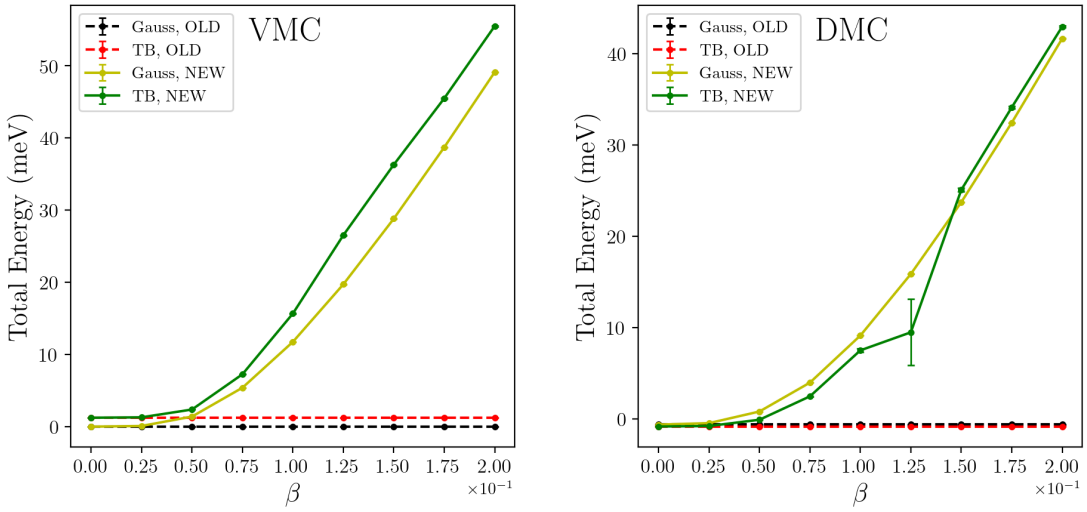

Figure 5.13. Comparison of total energies plotted against leak term β of new gaussian basis function. The result of old basis function used as a reference line. The system is a triangular flake with zigzag edges (13 electrons, 7 up, 6 down), $s = 1.4$, $k = 0$ and $\rho = 25$ nm.

that it does not improve the ground state energies obtained from DMC calculations.

CHAPTER 6

NAGAOKA FERROMAGNETISM TRANSITION RESULTS

In this chapter, we present the results revealing Nagaoka ferromagnetism transition. The Nagaoka ferromagnetism is predicted within Hubbard model, with double occupancy not being allowed, and when there is an exactly one hole in the system (see Appendix F). Therefore, our system is at near half-filling, 42 sites with 41 electrons, and 42 electrons for comparison. A similar VMC/DMC procedure is performed as explained in Chapter 5. However, in this part, the potential depth V_0 value is changed instead of potential well radius ρ. We start directly with the analysis of spin-spin correlation function (explained in Chapter 5), as we observe how the spin structure changes depending on V_0 and total number of electrons N_e in the system. The results from different spin values S_Z are analysed in order to obtain the ground state of the system for a given V_0. In all calculations, the finite size effects are eliminated.

In Fig. 6.1, spin-spin correlation function g is shown as a function of potential depth V_0 for $N = 42$ sites, $\rho = 25$ nm and $k \neq 0$. Both $N_e = 42$ and $N_e = 41$ electron numbers are considered for half-filling and a single hole away from half-filling, respectively.[34] For these calculations, only maximum and minimum values of S_Z are considered to determine the ground state of the system. As shown in figure, half-filling system exhibits a transition from metallic to AFM phase around $V_0 \approx -18$ meV, and the system with $N_e = 41$ electrons shows a transition from metallic to FM phase around $V_0 \approx -30$ meV. The results suggest that the system should make a transition to AFM phase before subtracting a single electron. If the same figure is analyzed vertically, the system exhibits a transition from AFM to FM phase around $V_0 \approx -30$ meV when an electron is pulled away from the system as it is suggested in Nagaoka theorem. After $V_0 \approx -30$ meV, the transition maintains its stability. Although, at $\rho = 25$ nm, AG exhibits metallic-like behavior as predicted in[33], increasing effect of potential depth V_0 opens a way to have a localized behavior for the systems. To elucidate the intrinsic electronic and magnetic properties of the system, we analyze the pair density function, $p_{\sigma\sigma_0}(\mathbf{r}, \mathbf{r}_0)$, which quantifies the probability of locating an electron with spin σ at position $\mathbf{r}$ given the

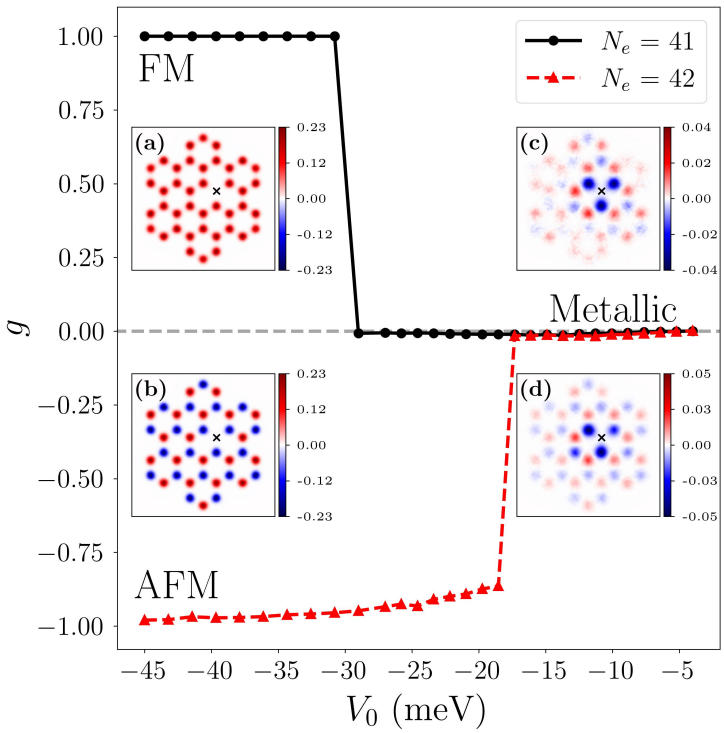

Figure 6.1. Extrapolated spin-spin correlation function plotted against potential depth V_0 obtained using pair densities for $N = 42$ sites, potential radius $\rho = 25$ nm and $k = 3.56 \times 10^{-4}$ meV/nm^2. Inset figures are extrapolated spin pair densities in the ground states. (a) $N_e = 41$, $V_0 \approx -45$ meV, $S_Z = 41/2$. (b) $N_e = 42$, $V_0 \approx -45$ meV, $S_Z = 0$. (c) $N_e = 41$, $V_0 \approx -8.84$ meV, $S_Z = 1/2$. (d) $N_e = 42$, $V_0 \approx -8.84$ meV, $S_Z = 0$.

presence of a reference electron with spin σ_0 at $\mathbf{r}_0$. Furthermore, we examine the pair spin density contrast, defined as $p_{\uparrow\uparrow}(\mathbf{r}, \mathbf{r}_0) - p_{\downarrow\uparrow}(\mathbf{r}, \mathbf{r}_0)$, to capture the spin-dependent spatial correlations. Figures 6.1a-b-c-d depict these pair spin densities for a reference spin-down electron positioned atop a lattice site-strategically chosen to break system symmetry while avoiding edge effects-denoted by a cross. In Fig. 6.1a, the system have a fully FM phase for $N_e = 41$ electrons at $V_0 = -45$ meV with maximum $S_Z = 41/2$ while the system with $N_e = 42$ electrons at the same V_0 value Fig. 6.1b exhibits an AFM phase at minimum $S_Z = 0$. Additionally, at the lower extrema value of $V_0 \approx -8.84$ meV, Fig. 6.1c and 6.1d shows metallic phases for $N_e = 41$ with $S_Z = 1/2$ and $N_e = 42$ with $S_Z = 0$, respectively. Thus, spin pair density calculations reinforces of the predictions of spin-spin correlation function calculations.

In Fig. 6.2, we turn our attention to more localized systems in which potential

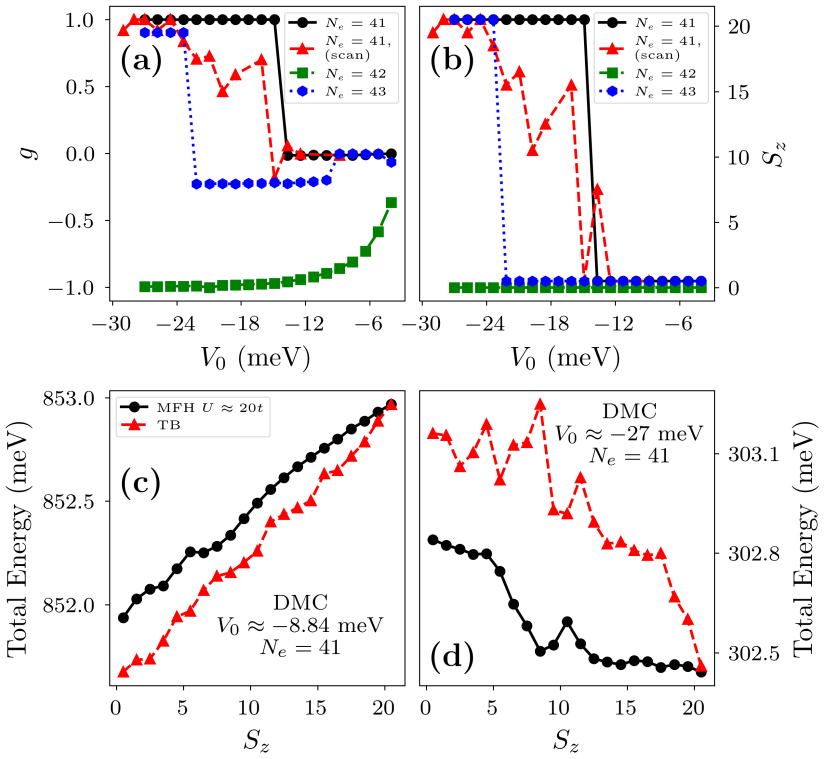

Figure 6.2. (a) Extrapolated spin-spin correlation function plotted against potential depth V_0 obtained using pair densities for $N = 42$ sites, potential radius $\rho = 17.5$ nm and $k = 3.56 \times 10^{-4}$ meV/nm^2. (b) Ground state spin S_Z values plotted against potential depth V_0. (c) DMC energies plotted against S_z at $V_0 \approx -8.84$ meV for $N_e = 41$. (d) DMC energies plotted against S_z at $V_0 \approx -27$ meV for $N_e = 41$.

radius $\rho = 17.5$ nm, in order to strengthen the electron correlations.[33] Fig. 6.2a shows spin-spin correlation function as a function of V_0 for $N_e = 41$, $N_e = 42$ and $N_e = 43$ electrons. In order to validate the results in more detail, a full spin S_Z scan have been also performed for $N_e = 41$ to determine the ground states of the system for a given V_0. In contrast to Fig. 6.1, half-filling system already shows an AFM behavior starting from higher V_0 values shown in Fig. 6.2a, which is directly correlated with potential radius $\rho = 17.5$ nm used in these calculations. The ground states determined from extrema S_Z values are indicated as S_Z-min/max. From S_Z-min/max calculations of $N_e = 41$ electrons, it is observed that the sharp transition from metallic to FM phase is at higher value $V_0 \approx -15$ meV than $\rho = 25$ nm case. Thus, an AFM to FM phase transition also occurs in $\rho = 17.5$ nm system depending on electron number yet in a higher V_0 value effected by strong

electron-electron interactions. Full S_Z-scan of $N_e = 41$ electrons shows a smoother transition starting from $V_0 \approx -15$ meV, ignoring statistical fluctuations emerging from DMC calculations. It is fully polarized FM phase around $V_0 \approx -26$ meV. Fig. 6.2b-c show DMC total energies at two examples of extrema V_0 values of -8.84 meV and -27 meV for $N_e = 41$ electrons. MFH $U \approx 20t$ trial wave functions represents more localized states, and TB trial wave functions represents liquid-like states. As seen from Fig. 6.2c, the lowest energy is given by the TB trial wave function at $S_Z = 1/2$ for $V_0 \approx -8.84$ meV. In Fig. 6.2d, the ground state is represented by the MFH $U \approx 20t$ trial wave function at $S_Z = 41/2$ for $V_0 \approx -27$ meV. In Fig. 6.2a, we also show $N_e = 43$ electrons results in which the system first exhibits a low AFM phase then exhibits a transition to FM state around $V_0 \approx -23$ meV. Although, g seems around 0.9 for $N_e = 43$ electrons, in Fig. 6.2b shows a fully polarized FM phase. The spin-spin correlation function seems lower since there is an additional opposite spin electron in the system. Therefore, the AFM to FM phase transition also occurs by adding one electron to the system, as suggested by Nagaoka theorem.[34]

In Fig. 6.3, extrapolated spin pair densities for $N_e = 41$ electrons on $N = 42$ sites are shown at several potential depth V_0 values being chosen to reveal the nature of the phase transition. While a liquid-like state is seen from Fig. 6.3a at a high V_0 value, a fully polarized FM state is observed around $V_0 \approx -27$ meV (Fig. 6.3d), consistent with g values shown in Fig. 6.2a. An important point is that before going into a phase transition to FM state, the system exhibits an AFM state around $V_0 \approx -14.89$ meV due to increasing electron-electron correlations, as seen from Fig. 6.3b. During the transition around $V_0 \approx -19.74$ meV in Fig. 6.3c, the polarization of spins located more around the center. This behavior hints a possible Nagaoka polaron formation in AG systems.

In order to reveal the intrinsic strength of electron-electron interactions, the onsite Coulomb interaction, U, and the hopping parameter, t, are calculated as explained in Chapter 2. As shown in Fig. 6.4, the ratio U/t is increasing in an exponential fashion as V_0 decreases. The exponential increase of U/t is a direct consequence of increasing U and decreasing t for decreasing V_0, shown in Fig. 6.4a and 6.4b. Around the starting point of AFM to FM phase transition, $V_0 \approx -15$, the ratio $U/t \approx 60$ while around end point, $V_0 \approx -26$, the ratio $U/t \approx 170$. High values of the ratio U/t is in agreement with Nagaoka theorem in which double occupation is restricted on sites.

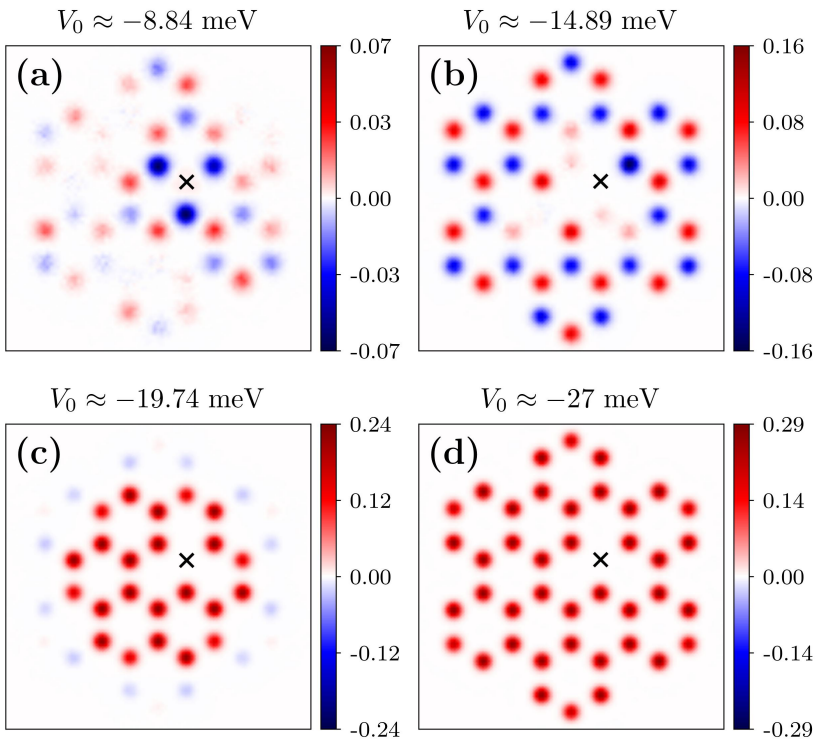

Figure 6.3. Extrapolated spin pair densities for $N_e = 41$ electrons on $N = 42$ sites at several potential depth V_0 values. (a) $V_0 \approx -8.84$ meV. (b) $V_0 \approx -14.89$ meV. (c) $V_0 \approx -19.74$ meV. (d) $V_0 \approx -27$ meV.

In order to analyze another flake size, additional QMC calculations is performed for $N_e = 113$ electrons in $N = 114$ sites for a hexagonal armchair flake. All S_z values are scanned for two potential depth V_0 values since full many-body calculations of 113 electrons are computationally expensive. In Fig. 6.5, QMC pair spin density results are shown for (a) $V_0 \approx -20$ meV, and (b) $V_0 \approx -30$ meV. V_0 values are chosen using S_z scan results of $N = 41$ electrons (a value after the transition, and a value during the transition). For both potential depth values, the total energies result in similar values within error bars. Since the ground state cannot be determined, an ensemble average is calculated using Boltzmann distribution at $T = 4$ K. For both cases, it is seen that FM state starts to build up. In Fig. 6.5a, $g \approx 0.65$ and $S_z \approx 46.26$, g has an intermediate value during the transition as predicted. For Fig. 6.5b, g is closer to the fully polarized phase, as $g \approx 0.79$ and $S_z \approx 50.37$.

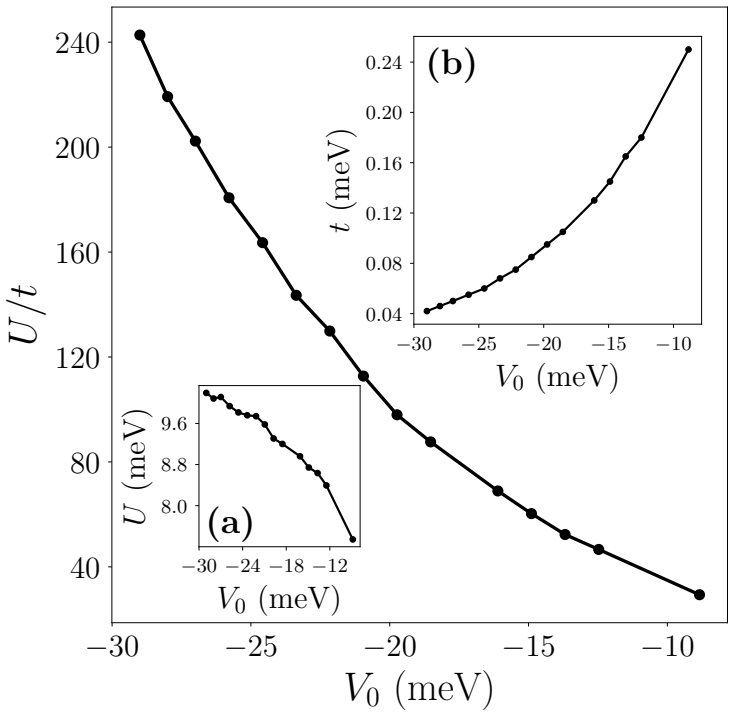

Figure 6.4. The ratio of onsite Coulomb interaction U to nearest-neighbor hopping parameter t, U/t, plotted against V_0 for $\rho = 17.5$ nm and $k = 3.56 \times 10^{-4}$ meV/nm^2. (a) U vs. V_0. (b) t vs. V_0.

6.1. Summary

An hexagonal armchair flake with 42 sites is analyzed using VMC/DMC methods. Spin-spin correlation values are obtained as potential depth V_0 changes for a given potential well radius ρ, and electron number N_e. In order to represent the ground states, minimum energies are chosen from different S_Z values and trial wave functions. The finite size effects are eliminated. We conclude that the hexagonal armchair AG flake with 42 sites exhibits an AFM to FM transition with respect to electron number (AFM phase for 42 electrons, FM phase for 41 electrons). However, we observed that before the system goes into FM regime, it should be in an AFM phase. The ratio of onsite Coulomb interaction U to nearest-neighbor hopping parameter t, U/t, is predicted from the solutions of single particle Schrödinger equations, TB, and QMC methods. The transition happens in a region $U/t \approx 60 - 170$ which indicates strong electron interactions are necessary.

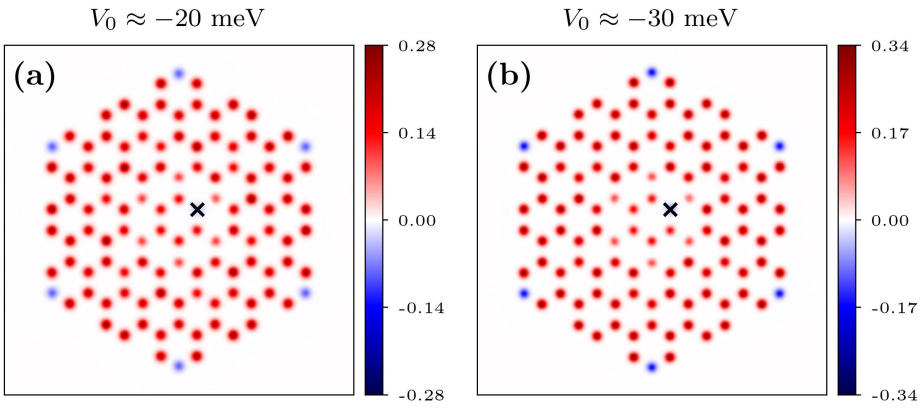

Figure 6.5. QMC pair spin density results for $N_e = 113$ electrons in $N = 114$ sites from full S_z scan. The results are ensemble averages at $T = 4$ K since the total energies obtained from all S_z values are similar within error bars. (a) $V_0 \approx -20$ meV, $g \approx 0.65$, $S_z \approx 46.26$. (b) $V_0 \approx -30$ meV, $g \approx 0.79$, $S_z \approx 50.37$.

CHAPTER 7

CONCLUSION

Firstly, we have modelled a quantum simulator in which a nanopatterned artificial graphene system on GaAs based quantum wells with lattice constant $a = 50$ nm is formed. Depth of the potentials V_0 were tuned so that the system remains charge neutral within Lieb's theorem. Dirac cones observed on all V_0 values by density functional theory calculations which validated the reliability of the potential depth values. Accurate variational and diffusion Monte Carlo calculations have been performed using several trial wave functions for systematic investigation of quantum well shape, dot radius, system size and effect of gate potentials. We have shown that a simple tight-binding trial wave function combined with Jastrow factor is sufficient for electron correlation effects in both metallic and antiferromagnetic regimes. Moreover, quantum Monte Carlo results predicted that semiconductor hexagonal artificial graphene flake with armchair edges exhibit a metallic to antiferromagnetic insulator phase transition depending on quantum dot radius, and almost independent from the sharpness of the potential wells and the system size, as shown in Chapter 5. We confirmed our calculations by placing a quadratic gate potential at the center of the system in order to preserve uniform electron distribution. The phase transition exists on both results with or without gate potential, around $\rho \approx 26$ nm and $\rho \approx 18$ nm respectively for 42 sites (42 electrons). It is around $\rho \approx 16$ nm for 114 sites (114 electrons) without the gate potential. The fact that the phase transition does not depend on potential sharpness, system size or charge uniformity strengthened our predictions on existence of the metal - antiferromagnetic insulator transition. The results are consistent with the calculations on triangular AG flake with zigzag edges, in which a similar behavior is observed.[33] Similar to predictions on real graphene quantum dots, AG quantum dots also displays distinct magnetic states that increases its value in order to simulate graphene quantum dots as good practical quantum simulators.

Secondly, we have implemented the method required for using orbital coefficients other than Gaussian orbitals, in other words, non-diagonal orbital coeffient matrices, as mentioned in Chapter 3. We extended the variational Monte Carlo method to optimize the

trial wave functions including orbital coefficients obtained from tight-binding or mean-field Hubbard calculations yet not constrained to those two methods. We have shown that the new implementation both smooths out the optimization process and yields lower energies compared to original algorithm. The new method allows more possibilities of trial wave functions to optimize with variational Monte Carlo, i.e. increases the number of distinct nodal structures that we provide for diffusion Monte Carlo.

Lastly, a new basis function have been used for generating a more flexible nodal structure than the nodal structure of Gaussian basis function. This new basis function, so-called "leaky" gaussian function, has one more additional parameter that can alter the nodal surfaces. However, we have shown that the leaky Gaussian basis function did not improve the variational or diffusion Monte Carlo energies, in fact it introduced more statistical fluctuations for diffusion Monte Carlo, and always results in higher energies for both methods, as shown in section 5.4. Therefore, the original Gaussian basis function would be the most suitable basis function for quantum dots on hexagonal lattice structures.

Moreover, we demonstrated that Nagaoka ferromagnetism can be probed in semiconductor artificial graphene nanostructures using accurate variational and diffusion Monte Carlo calculations, alongside exact diagonalization of the Hubbard model, as mentioned in Chapter 6. Specifically, quantum Monte Carlo calculations in the subspaces of minimum and maximum polarization for a potential radius $\rho = 25$ nm on $N = 42$ sites near half-filling reveal a sharp antiferromagnetic to ferromagnetic phase transition around potential depth of $V_0 \approx -30$ meV, driven by the absence of a single electron. For $\rho = 17.5$ nm, a similar transition occurs, though a full scan over S_Z values exhibits a smoother transition, beginning at $V_0 \approx -15$ meV when an electron is removed. Additionally, the phase transition can be induced by adding an electron, consistent with Nagaoka's theorem. As V_0 decreases, the $N_e = 41$ electron system evolves from a liquid-like state to a fully ferromagnetic phase, passing through an intermediate antiferromagnetic phase where spin polarization gradually builds near the system's center, suggesting possible Nagaoka polaron formation. By combining results from quantum Monte Carlo, single-particle Schrödinger equation solutions, and tight-binding Hamiltonian diagonalization, we estimate the ratio of onsite Coulomb interaction U to nearest-neighbor hopping parameter t, finding the phase transition to occur within $U/t \approx 60$-170, indicating strong electron correlation is necessary. Thus, our findings establish, covering full long-range interactions, the pres-

ence of an antiferromagnetic to ferromagnetic phase transition in semiconductor artificial graphene nanostructured on GaAs quantum wells, governed both by electron removal and by tuning the potential depth V_0.

REFERENCES

1. Wallace, P. R. The Band Theory of Graphite. *Phys. Rev.* **1947**, *71*, 622–634.

2. Dirac, P. A. The quantum theory of the electron. *Proc. R. Soc. Lond. A* **1928**, *117*, 610–624.

3. Weyl, H. GRAVITATION AND THE ELECTRON. *Proceedings of the National Academy of Sciences* **1929**, *15*, 323–334.

4. Zhou, S. Y.; Gweon, G.-H.; Graf, J.; Fedorov, A. V.; Spataru, C. D.; Diehl, R. D.; Kopelevich, Y.; Lee, D.-H.; Louie, S. G.; Lanzara, A. First direct observation of Dirac fermions in graphite. *Nature Physics* **2006**, *2*, 595–599.

5. Sadowski, M. L.; Martinez, G.; Potemski, M.; Berger, C.; de Heer, W. A. Landau Level Spectroscopy of Ultrathin Graphite Layers. *Phys. Rev. Lett.* **2006**, *97*, 266405.

6. Geim, A. K. Nobel Lecture: Random walk to graphene. *Rev. Mod. Phys.* **2011**, *83*, 851–862.

7. Novoselov, K. S.; Jiang, Z.; Zhang, Y.; Morozov, S. V.; Stormer, H. L.; Zeitler, U.; Maan, J. C.; Boebinger, G. S.; Kim, P.; Geim, A. K. Room-temperature quantum Hall effect in graphene. *Science* **2007**, *315*, 1379.

8. Geim, A. K.; Novoselov, K. S. The rise of graphene. *Nature Materials* **2007**, *6*, 183–191.

9. Katsnelson, M. I.; Novoselov, K. S.; Geim, A. K. Chiral tunnelling and the Klein paradox in graphene. *Nature Physics* **2006**, *2*, 620–625.

10. Katsnelson, M. I. Graphene: carbon in two dimensions. *Materials Today* **2007**, *10*, 20–27.

11. Güçlü, A. D.; Potasz, P.; Korkusinski, M.; Hawrylak, P. *Graphene Quantum Dots*;

Springer: Berlin, Heidelberg, 2014.

12. Su, J., et al. Atomically precise bottom-up synthesis of π-extended [5]triangulene. *Sci. Adv.* **2019**, *5*, eaav7717.

13. Sun, Y.; Zheng, Y.; Pan, H.; Chen, J.; Zhang, W.; Fu, L.; Zhang, K.; Tang, N.; Du, Y. Magnetism of graphene quantum dots. *npj Quantum Materials* **2017**, *2*, 5.

14. Ruffieux, P.; Wang, S.; Yang, B.; Sánchez-Sánchez, C.; Liu, J.; Dienel, T.; Talirz, L.; Shinde, P.; Pignedoli, C. A.; Passerone, D.; Dumslaff, T.; Feng, X.; Müllen, K.; Fasel, R. On-surface synthesis of graphene nanoribbons with zigzag edge topology. *Nature* **2016**, *531*, 489–492.

15. Du, L., et al. Emerging many-body effects in semiconductor artificial graphene with low disorder. *Nat. Commun.* **2018**, *9*, 3299.

16. Wang, S., et al. Observation of Dirac bands in artificial graphene in small-period nanopatterned GaAs quantum wells. *Nat. Nanotechnol.* **2018**, *13*, 29–33.

17. Gibertini, M.; Singha, A.; Pellegrini, V.; Polini, M.; Vignale, G.; Pinczuk, A.; Pfeiffer, L. N.; West, K. W. Engineering artificial graphene in a two-dimensional electron gas. *Phys. Rev. B* **2009**, *79*, 241406.

18. Räsänen, E.; Rozzi, C. A.; Pittalis, S.; Vignale, G. Electron-Electron Interactions in Artificial Graphene. *Phys. Rev. Lett.* **2012**, *108*, 246803.

19. Kylänpää, I.; Aichinger, M.; Janecek, S.; Räsänen, E. Finite-size effects and interactions in artificial graphene formed by repulsive scatterers. *J. Phys. Condens. Matter* **2015**, *27*, 425501.

20. Kylänpää, I.; Berardi, F.; Räsänen, E.; García-González, P.; Rozzi, C. A.; Rubio, A. Stability of the Dirac cone in artificial graphene formed in quantum wells: a computational many-electron study. *New J. Phys.* **2016**, *18*, 083014.

21. Assaad, F. F.; Herbut, I. F. Pinning the Order: The Nature of Quantum Criticality in the Hubbard Model on Honeycomb Lattice. *Phys. Rev. X* **2013**, *3*, 031010.

22. Otsuka, Y.; Yunoki, S.; Sorella, S. Universal Quantum Criticality in the Metal-Insulator Transition of Two-Dimensional Interacting Dirac Electrons. *Phys. Rev. X* **2016**, *6*, 011029.

23. Buividovich, P.; Smith, D.; Ulybyshev, M.; von Smekal, L. Numerical evidence of conformal phase transition in graphene with long-range interactions. *Phys. Rev. B* **2019**, *99*, 205434.

24. Ostmeyer, J.; Berkowitz, E.; Krieg, S.; Lähde, T. A.; Luu, T.; Urbach, C. Semimetal–Mott insulator quantum phase transition of the Hubbard model on the honeycomb lattice. *Phys. Rev. B* **2020**, *102*, 245105.

25. Saleem, Y.; Dusko, A.; Cygorek, M.; Korkusinski, M.; Hawrylak, P. Quantum simulator of extended bipartite Hubbard model with broken sublattice symmetry: Magnetism, correlations, and phase transitions. *Phys. Rev. B* **2022**, *105*, 205105.

26. McMillan, W. L. Ground State of Liquid He^4. *Phys. Rev.* **1965**, *138*, A442–A451.

27. Ceperley, D.; Chester, G. V.; Kalos, M. H. Monte Carlo simulation of a many-fermion study. *Phys. Rev. B* **1977**, *16*, 3081–3099.

28. Kalos, M. H. Monte Carlo Calculations of the Ground State of Three- and Four-Body Nuclei. *Phys. Rev.* **1962**, *128*, 1791–1795.

29. Kalos, M. H.; Levesque, D.; Verlet, L. Helium at zero temperature with hard-sphere and other forces. *Phys. Rev. A* **1974**, *9*, 2178–2195.

30. Tanatar, B.; Ceperley, D. M. Ground state of the two-dimensional electron gas. *Phys. Rev. B* **1989**, *39*, 5005–5016.

31. Foulkes, W. M. C.; Mitas, L.; Needs, R. J.; Rajagopal, G. Quantum Monte Carlo sim-

ulations of solids. *Rev. Mod. Phys.* **2001**, *73*, 33–83.

32. Güçlü, A. D.; Jeon, G. S.; Umrigar, C. J.; Jain, J. K. Quantum Monte Carlo study of composite fermions in quantum dots: The effect of Landau-level mixing. *Phys. Rev. B* **2005**, *72*, 205327.

33. Öztarhan, G.; Kul, E. B.; Okcu, E.; Güçlü, A. D. Quantum Monte Carlo study of semiconductor artificial graphene nanostructures. *Phys. Rev. B* **2023**, *108*, L161114.

34. Öztarhan, G.; Potasz, P.; Güçlü, A. D. Nagaoka ferromagnetism in semiconductor artificial graphene. 2025.

35. Nagaoka, Y. Ferromagnetism in a Narrow, Almost Half-Filled s Band. *Phys. Rev.* **1966**, *147*, 392–405.

36. Tasaki, H. Extension of Nagaoka's theorem on the large-U Hubbard model. *Phys. Rev. B* **1989**, *40*, 9192–9193.

37. Dehollain, J. P.; Mukhopadhyay, U.; Michal, V. P.; Wang, Y.; Wunsch, B.; Reichl, C.; Wegscheider, W.; Rudner, M. S.; Demler, E.; Vandersypen, L. M. K. Nagaoka ferromagnetism observed in a quantum dot plaquette. *Nature* **2020**, *579*, 528–533.

38. Botzung, T.; Nataf, P. Numerical observation of SU(N) Nagaoka ferromagnetism. *Phys. Rev. B* **2024**, *109*, 235131.

39. Li, Y.; Liu, K.; Bryant, G. W. Nagaoka ferromagnetism in 3×3 arrays and beyond. *Phys. Rev. B* **2024**, *110*, 245141.

40. Becca, F.; Sorella, S. Nagaoka Ferromagnetism in the Two-Dimensional Infinite- U Hubbard Model. *Phys. Rev. Lett.* **2001**, *86*, 3396–3399.

41. Emery, V. J.; Kivelson, S. A.; Lin, H. Q. Phase separation in the t-J model. *Phys. Rev. Lett.* **1990**, *64*, 475–478.

42. Liu, L.; Yao, H.; Berg, E.; White, S. R.; Kivelson, S. A. Phases of the Infinite U

Hubbard Model on Square Lattices. *Phys. Rev. Lett.* **2012**, *108*, 126406.

43. Shastry, B. S.; Krishnamurthy, H. R.; Anderson, P. W. Instability of the Nagaoka ferromagnetic state of the U=∞ Hubbard model. *Phys. Rev. B* **1990**, *41*, 2375–2379.

44. White, S. R.; Affleck, I. Density matrix renormalization group analysis of the Nagaoka polaron in the two-dimensional $t - J$ model. *Phys. Rev. B* **2001**, *64*, 024411.

45. Park, H.; Haule, K.; Marianetti, C. A.; Kotliar, G. Dynamical mean-field theory study of Nagaoka ferromagnetism. *Phys. Rev. B* **2008**, *77*, 035107.

46. Fang, Y.; Ruckenstein, A. E.; Dagotto, E.; Schmitt-Rink, S. Holes in the infinite-U Hubbard model: Instability of the Nagaoka state. *Phys. Rev. B* **1989**, *40*, 7406–7409.

47. Westerhout, T.; Katsnelson, M. I. Role of correlated hopping in the many-body physics of flat-band systems: Nagaoka ferromagnetism. *Phys. Rev. B* **2022**, *106*, L041104.

48. Samajdar, R.; Bhatt, R. N. Polaronic mechanism of Nagaoka ferromagnetism in Hubbard models. *Phys. Rev. B* **2024**, *109*, 235128.

49. Wang, Y.; Dehollain, J. P.; Liu, F.; Mukhopadhyay, U.; Rudner, M. S.; Vandersypen, L. M. K.; Demler, E. Ab initio exact diagonalization simulation of the Nagaoka transition in quantum dots. *Phys. Rev. B* **2019**, *100*, 155133.

50. Morales-Durán, N.; Hu, N. C.; Potasz, P.; MacDonald, A. H. Nonlocal interactions in moiré Hubbard systems. *Physical Review Letters* **2022**, *128*, 217202.

51. Umrigar, C. J.; Filippi, C. Energy and Variance Optimization of Many-Body Wave Functions. *Phys. Rev. Lett.* **2005**, *94*, 150201.

52. Metropolis, N.; Ulam, S. The Monte Carlo Method. *Journal of the American Statistical Association* **1949**, *44*, 335–341, PMID: 18139350.

53. Metropolis, N.; Rosenbluth, A. W.; Rosenbluth, M. N.; Teller, A. H.; Teller, E. Equa-

tion of State Calculations by Fast Computing Machines. *The Journal of Chemical Physics* **1953**, *21*, 1087–1092.

54. Hastings, W. K. Monte Carlo sampling methods using Markov chains and their applications. *Biometrika* **1970**, *57*, 97–109.

55. Umrigar, C. J. Accelerated Metropolis method. *Phys. Rev. Lett.* **1993**, *71*, 408–411.

56. Toulouse, J.; Assaraf, R.; Umrigar, C. J. In *Electron Correlation in Molecules – ab initio Beyond Gaussian Quantum Chemistry*; Hoggan, P. E., Ozdogan, T., Eds.; Advances in Quantum Chemistry; Academic Press, 2016; Vol. 73; pp 285–314.

57. Umrigar, C. J.; Toulouse, J.; Filippi, C.; Sorella, S.; Hennig, R. G. Alleviation of the Fermion-Sign Problem by Optimization of Many-Body Wave Functions. *Phys. Rev. Lett.* **2007**, *98*, 110201.

58. Umrigar, C. J.; Wilson, K. G.; Wilkins, J. W. Optimized trial wave functions for quantum Monte Carlo calculations. *Phys. Rev. Lett.* **1988**, *60*, 1719–1722.

59. Umrigar, C. J.; Nightingale, M. P.; Runge, K. J. A diffusion Monte Carlo algorithm with very small time-step errors. *J. Chem. Phys.* **1993**, *99*, 2865–2890.

60. Filippi, C.; Umrigar, C. J. Multiconfiguration wave functions for quantum Monte Carlo calculations of first-row diatomic molecules. *The Journal of Chemical Physics* **1996**, *105*, 213–226.

61. Ceperley, D. Ground state of the fermion one-component plasma: A Monte Carlo study in two and three dimensions. *Phys. Rev. B* **1978**, *18*, 3126–3138.

62. Ghosal, A.; Güçlü, A. D.; Umrigar, C. J.; Ullmo, D.; Baranger, H. U. Correlation-induced inhomogeneity in circular quantum dots. *Nat. Phys.* **2006**, *2*, 336–340.

63. Güçlü, A. D.; Umrigar, C. J.; Jiang, H.; Baranger, H. U. Localization in an inhomogeneous quantum wire. *Phys. Rev. B* **2009**, *80*, 201302.

64. Filippi, C.; Assaraf, R.; Moroni, S. Simple formalism for efficient derivatives and multi-determinant expansions in quantum Monte Carlo. *The Journal of Chemical Physics* **2016**, *144*, 194105.

65. Fernández-Rossier, J.; Palacios, J. J. Magnetism in Graphene Nanoislands. *Phys. Rev. Lett.* **2007**, *99*, 177204.

66. Potasz, P.; Güçlü, A. D.; Wójs, A.; Hawrylak, P. Electronic properties of gated triangular graphene quantum dots: Magnetism, correlations, and geometrical effects. *Phys. Rev. B* **2012**, *85*, 075431.

67. Lieb, E. H. Two theorems on the Hubbard model. *Phys. Rev. Lett.* **1989**, *62*, 1201–1204.

APPENDIX A

DERIVATIVES OF VARIATIONAL ENERGY AND VARIANCE WITH RESPECT TO FREE PARAMETERS

In this chapter, we provide detailed derivation of the parameters derivatives of the variational energy and the variance. For the sake of simplicity and readability, the following notations are used.

$$\begin{aligned}
\Psi &\equiv \Psi_T \\
E_L &= \frac{\hat{H}\Psi}{\Psi} \\
\overline{E} &= \frac{\langle \Psi | \hat{H} | \Psi \rangle}{\langle \Psi | \Psi \rangle} = \frac{\int \Psi^* \hat{H} \Psi d\mathrm{R}}{\int \Psi^* \Psi d\mathrm{R}} \\
\Psi_\alpha &= \frac{\partial}{\partial \alpha} \Psi
\end{aligned}$$

In addition to the notations above, the notation $\langle \bullet \rangle_{|\Psi|^2}$ means Monte Carlo average using the $|\Psi|^2$ distribution i.e.

$$\langle \Phi \rangle_{|\Psi|^2} \equiv \int \frac{|\Psi|^2}{\int |\Psi|^2 d\mathrm{R}} \Phi d\mathrm{R}.$$

A.0.1. Gradient of Energy

Let us examine the first derivative of the variational energy with respect to free parameter α.

$$\overline{E}_\alpha = \frac{\int \Psi_\alpha^* \hat{H}\Psi d\mathrm{R}}{\int \Psi^*\Psi d\mathrm{R}} + \frac{\int \Psi^* \hat{H}\Psi_\alpha d\mathrm{R}}{\int \Psi^*\Psi d\mathrm{R}} - \frac{\int \Psi_\alpha^*\Psi d\mathrm{R} \int \Psi^*\hat{H}\Psi d\mathrm{R}}{(\int \Psi^*\Psi d\mathrm{R})^2} - \frac{\int \Psi^*\Psi_\alpha d\mathrm{R} \int \Psi^*\hat{H}\Psi d\mathrm{R}}{(\int \Psi^*\Psi d\mathrm{R})^2}.$$

If we rearrange the last two terms, the gradient becomes

$$\overline{E}_\alpha = \frac{\int \Psi_\alpha^* \hat{H}\Psi d\mathrm{R}}{\int \Psi^*\Psi d\mathrm{R}} + \frac{\int \Psi^* \hat{H}\Psi_\alpha d\mathrm{R}}{\int \Psi^*\Psi d\mathrm{R}} - \frac{\int \Psi_\alpha^*\Psi d\mathrm{R}}{\int \Psi^*\Psi d\mathrm{R}}\overline{E} - \frac{\int \Psi^*\Psi_\alpha d\mathrm{R}}{\int \Psi^*\Psi d\mathrm{R}}\overline{E}. \tag{A.1}$$

Let us split it to four terms and rearrange them for Monte Carlo sampling.

- $\frac{\int \Psi_\alpha^* \hat{H}\Psi d\mathrm{R}}{\int \Psi^*\Psi d\mathrm{R}} = \frac{\int \Psi_\alpha^* \frac{\Psi^*}{\Psi^*}\frac{\Psi}{\Psi}\hat{H}\Psi d\mathrm{R}}{\int \Psi^*\Psi d\mathrm{R}} = \int \frac{\Psi^*\Psi}{\int \Psi^*\Psi d\mathrm{R}}\frac{\Psi_\alpha^*}{\Psi^*}\frac{\hat{H}\Psi}{\Psi}d\mathrm{R}$
- $\frac{\int \Psi^* \hat{H}\Psi_\alpha d\mathrm{R}}{\int \Psi^*\Psi d\mathrm{R}} = \frac{\int \Psi^* \frac{\Psi}{\Psi}\hat{H}\Psi_\alpha d\mathrm{R}}{\int \Psi^*\Psi d\mathrm{R}} = \int \frac{\Psi^*\Psi}{\int \Psi^*\Psi d\mathrm{R}}\frac{\hat{H}\Psi_\alpha}{\Psi}d\mathrm{R}$
- $\frac{\int \Psi_\alpha^*\Psi d\mathrm{R}}{\int \Psi^*\Psi d\mathrm{R}} = \frac{\int \Psi_\alpha^* \frac{\Psi^*}{\Psi^*}\Psi d\mathrm{R}}{\int \Psi^*\Psi d\mathrm{R}} = \int \frac{\Psi^*\Psi}{\int \Psi^*\Psi d\mathrm{R}}\frac{\Psi_\alpha^*}{\Psi^*}d\mathrm{R}$
- $\frac{\int \Psi^*\Psi_\alpha d\mathrm{R}}{\int \Psi^*\Psi d\mathrm{R}} = \frac{\int \Psi^* \frac{\Psi}{\Psi}\Psi_\alpha d\mathrm{R}}{\int \Psi^*\Psi d\mathrm{R}} = \int \frac{\Psi^*\Psi}{\int \Psi^*\Psi d\mathrm{R}}\frac{\Psi_\alpha}{\Psi}d\mathrm{R}.$

Inserting the four terms above into equation A.1 gives us

$$\overline{E}_\alpha = \int \frac{\Psi^*\Psi}{\int \Psi^*\Psi d\mathrm{R}}\left(\frac{\Psi_\alpha^*}{\Psi^*}E_L + \frac{\hat{H}\Psi_\alpha}{\Psi} - \frac{\Psi_\alpha^*}{\Psi^*}\overline{E} - \frac{\Psi_\alpha}{\Psi}\overline{E}\right)d\mathrm{R}.$$

Let us choose Ψ a real-valued function. The gradient becomes

$$\begin{aligned}\overline{E}_\alpha &= \int \frac{\Psi^*\Psi}{\int \Psi^*\Psi d\mathrm{R}} \left(\frac{\Psi_\alpha}{\Psi} E_L + \frac{\hat{H}\Psi_\alpha}{\Psi} - 2\overline{E}\frac{\Psi_\alpha}{\Psi} \right) d\mathrm{R} \\ &= \left\langle \frac{\Psi_\alpha}{\Psi} E_L + \frac{\hat{H}\Psi_\alpha}{\Psi} - 2\overline{E}\frac{\Psi_\alpha}{\Psi} \right\rangle_{|\Psi^2|} . \end{aligned} \tag{A.2}$$

Equation A.2 can be improved further to have smaller fluctuations. Since we use Monte Carlo techniques to sample the terms inside the brackets from $|\Psi|^2$ distribution, the gradient has also have a statistical error depending on the number of samples. The statistical error can be reduced with a more simpler form; starting from equation A.1 in Dirac notation

$$\overline{E}_\alpha = \frac{\langle \Psi_\alpha | \hat{H} | \Psi \rangle + \langle \Psi | \hat{H} | \Psi_\alpha \rangle - \langle \Psi_\alpha | \Psi \rangle \overline{E} - \langle \Psi | \Psi_\alpha \rangle \overline{E}}{\langle \Psi | \Psi \rangle},$$

using the Hermiticity of the Hamiltonian[51] it becomes

$$\overline{E}_\alpha = 2\frac{\langle \Psi_\alpha | \hat{H} | \Psi \rangle - \langle \Psi | \Psi_\alpha \rangle \overline{E}}{\langle \Psi | \Psi \rangle} = 2 \left\langle \frac{\Psi_\alpha}{\Psi} (E_L - \overline{E}) \right\rangle_{|\Psi^2|} .$$

A.0.2. Hessian Matrix Elements of Energy

In this section, we will derive the Hessian matrix elements of variational energy. Let us start with $\overline{E}$ for a real-valued Ψ.

$$\overline{E}_\alpha = 2 \left\langle \frac{\Psi_\alpha}{\Psi} (E_L - \overline{E}) \right\rangle_{|\Psi^2|} = 2 \int \frac{\Psi^*\Psi}{\int \Psi^*\Psi d\mathrm{R}} \frac{\Psi_\alpha}{\Psi} (E_L - \overline{E}) = 2 \frac{\int \Psi_\alpha \Psi (E_L - \overline{E}) d\mathrm{R}}{\int \Psi \Psi d\mathrm{R}}$$

Therefore, the derivative of $\overline{E}$ with respect to a second free parameter β is

$$\overline{E}_{\alpha\beta} = 2\left[\frac{\int(\Psi_{\alpha\beta}\Psi + \Psi_\alpha\Psi_\beta)(E_L - \overline{E})d\mathbf{R} + \int \Psi_\alpha\Psi(E_{L,\beta} - \overline{E}_\beta)d\mathbf{R}}{\int|\Psi|^2 d\mathbf{R}} - \frac{2\int\Psi\Psi_\beta d\mathbf{R}\int\Psi_\alpha\Psi(E_L - \overline{E})d\mathbf{R}}{(\int|\Psi|^2 d\mathbf{R})^2}\right].$$

The last term can be written as $\left(\frac{\int\Psi\Psi_\beta d\mathbf{R}}{\int|\Psi|^2 d\mathbf{R}}\right)\overline{E}_\alpha$, making $\overline{E}_{\alpha\beta}$ as the following.

$$\overline{E}_{\alpha\beta} = 2\left[\frac{\int(\Psi_{\alpha\beta}\Psi + \Psi_\alpha\Psi_\beta)(E_L - \overline{E})d\mathbf{R} + \int \Psi_\alpha\Psi(E_{L,\beta} - \overline{E}_\beta)d\mathbf{R} - \overline{E}_\alpha\int\Psi\Psi_\beta d\mathbf{R}}{\int|\Psi|^2 d\mathbf{R}}\right].$$

Let us split the terms and rearrange them one by one (remember the Ψ is real-valued).

- $\dfrac{\int\Psi_{\alpha\beta}\Psi(E_L - \overline{E})d\mathbf{R}}{\int|\Psi|^2 d\mathbf{R}} = \dfrac{\int\frac{\Psi}{\Psi}\frac{\Psi}{\Psi}\Psi_{\alpha\beta}\Psi(E_L - \overline{E})d\mathbf{R}}{\int|\Psi|^2 d\mathbf{R}} = \int\dfrac{|\Psi|^2}{\int|\Psi|^2 d\mathbf{R}}\dfrac{\Psi_{\alpha\beta}}{\Psi}(E_L - \overline{E})d\mathbf{R}$
- $\dfrac{\int\Psi_\alpha\Psi_\beta(E_L - \overline{E})d\mathbf{R}}{\int|\Psi|^2 d\mathbf{R}} = \dfrac{\int\frac{\Psi}{\Psi}\frac{\Psi}{\Psi}\Psi_\alpha\Psi_\beta(E_L - \overline{E})d\mathbf{R}}{\int|\Psi|^2 d\mathbf{R}} = \int\dfrac{|\Psi|^2}{\int|\Psi|^2 d\mathbf{R}}\dfrac{\Psi_\alpha\Psi_\beta}{|\Psi|^2}(E_L - \overline{E})d\mathbf{R}$
- $\dfrac{\int\Psi_\alpha\Psi E_{L,\beta}d\mathbf{R}}{\int|\Psi|^2 d\mathbf{R}} = \int\dfrac{|\Psi|^2}{\int|\Psi|^2 d\mathbf{R}}\dfrac{\Psi_\alpha}{\Psi}E_{L,\beta}d\mathbf{R}$
- $\dfrac{\int\Psi_\alpha\Psi\overline{E}_\beta d\mathbf{R}}{\int|\Psi|^2 d\mathbf{R}} = \overline{E}_\beta\dfrac{\int\frac{\Psi}{\Psi}\frac{\Psi}{\Psi}\Psi_\alpha\Psi d\mathbf{R}}{\int|\Psi|^2 d\mathbf{R}} = \overline{E}_\beta\int\dfrac{|\Psi|^2}{\int|\Psi|^2 d\mathbf{R}}\dfrac{\Psi_\alpha}{\Psi}d\mathbf{R}$
- $\overline{E}_\alpha\dfrac{\int\Psi\Psi_\beta d\mathbf{R}}{\int|\Psi|^2 d\mathbf{R}} = \overline{E}_\alpha\int\dfrac{|\Psi|^2}{\int|\Psi|^2 d\mathbf{R}}\dfrac{\Psi_\beta}{\Psi}d\mathbf{R}$

Therefore, the Hessian matrix elements becomes

$$\overline{E}_{\alpha\beta} = 2\left[\left\langle\left(\frac{\Psi_{\alpha\beta}}{\Psi} + \frac{\Psi_\alpha\Psi_\beta}{|\Psi|^2}\right)(E_L - \overline{E})\right\rangle_{|\Psi|^2} - \overline{E}_\beta\left\langle\frac{\Psi_\alpha}{\Psi}\right\rangle_{|\Psi|^2} - \overline{E}_\alpha\left\langle\frac{\Psi_\beta}{\Psi}\right\rangle_{|\Psi|^2} + \left\langle\frac{\Psi_\alpha}{\Psi}E_{L,\beta}\right\rangle_{|\Psi|^2}\right]. \tag{A.3}$$

In order to reduce the variance of equation A.3, and to symmetrize the last term $\left\langle \frac{\Psi_\alpha}{\Psi} E_{L,\beta} \right\rangle_{|\Psi|^2}$, we make minor modifications to this equation. Note that

$$\begin{aligned}
\langle E_{L,\alpha} \rangle_{|\Psi|^2} &= \int \frac{|\Psi|^2}{\int |\Psi|^2 d\mathbf{R}} \frac{\partial}{\partial \alpha} \frac{\hat{H}\Psi}{\Psi} \\
&= \int \frac{|\Psi|^2}{\int |\Psi|^2 d\mathbf{R}} \left(\frac{\hat{H}\Psi_\alpha}{\Psi} - \frac{\Psi_\alpha}{|\Psi|^2} \hat{H}\Psi \right) d\mathbf{R} \\
&= \frac{\int (\Psi \hat{H} \Psi_\alpha - \Psi_\alpha \hat{H} \Psi)}{\int |\Psi|^2 d\mathbf{R}} = 0.
\end{aligned}$$

Thus, addition of the terms involving $\langle E_{L,\alpha} \rangle_{|\Psi|^2}$, such as $\left\langle \frac{\Psi_\beta}{\Psi} \right\rangle_{|\Psi|^2} \langle E_{L,\alpha} \rangle_{|\Psi|^2}$, does not change the overall result. Additionally, if $\sqrt{\langle a^2 \rangle - \langle a \rangle^2} << |\langle a \rangle|$ and $\langle b \rangle$ is small, the fluctuations of the covariance $\langle ab \rangle - \langle a \rangle \langle b \rangle$ are smaller than the fluctuations of $\langle ab \rangle$ (for our calculations $\langle b \rangle \equiv \langle E_{L,\alpha} \rangle_{|\Psi|^2} = 0$ for large enough finite sample size).[51] Therefore, we make the modification

$$\begin{aligned}
\left\langle \frac{\Psi_\alpha}{\Psi} E_{L,\beta} \right\rangle_{|\Psi|^2} \rightarrow \frac{1}{2} \Bigg(& \left\langle \frac{\Psi_\alpha}{\Psi} E_{L,\beta} \right\rangle_{|\Psi|^2} - \left\langle \frac{\Psi_\alpha}{\Psi} \right\rangle_{|\Psi|^2} \langle E_{L,\beta} \rangle_{|\Psi|^2} \\
& + \left\langle \frac{\Psi_\beta}{\Psi} E_{L,\alpha} \right\rangle_{|\Psi|^2} - \left\langle \frac{\Psi_\beta}{\Psi} \right\rangle_{|\Psi|^2} \langle E_{L,\alpha} \rangle_{|\Psi|^2} \Bigg).
\end{aligned}$$

The Hessian matrix elements become

$$\begin{aligned}
\overline{E}_{\alpha\beta} = 2 \Bigg[& \left\langle \left(\frac{\Psi_{\alpha\beta}}{\Psi} + \frac{\Psi_\alpha \Psi_\beta}{|\Psi|^2} \right) (E_L - \overline{E}) \right\rangle_{|\Psi|^2} - \overline{E}_\beta \left\langle \frac{\Psi_\alpha}{\Psi} \right\rangle_{|\Psi|^2} - \overline{E}_\alpha \left\langle \frac{\Psi_\beta}{\Psi} \right\rangle_{|\Psi|^2} \Bigg] \\
& + \left\langle \frac{\Psi_\alpha}{\Psi} E_{L,\beta} \right\rangle_{|\Psi|^2} - \left\langle \frac{\Psi_\alpha}{\Psi} \right\rangle_{|\Psi|^2} \langle E_{L,\beta} \rangle_{|\Psi|^2} + \left\langle \frac{\Psi_\beta}{\Psi} E_{L,\alpha} \right\rangle_{|\Psi|^2} - \left\langle \frac{\Psi_\beta}{\Psi} \right\rangle_{|\Psi|^2} \langle E_{L,\alpha} \rangle_{|\Psi|^2}.
\end{aligned} \tag{A.4}$$

A.0.3. Gradient and Hessian Matrix Elements of Variance

The variance of the variational energy is represented as

$$\sigma^2 = \frac{\int |\Psi|^2 (E_L - \overline{E})^2 d\mathbf{R}}{\int |\Psi|^2 d\mathbf{R}}$$

The gradient of the variance is the following.

$$\begin{aligned}
(\sigma^2)_\alpha &= \frac{\int 2\Psi\Psi_\alpha (E_L - \overline{E})^2 d\mathbf{R}}{\int |\Psi|^2 d\mathbf{R}} + \frac{\int |\Psi|^2 2(E_L - \overline{E})(E_{L,\alpha} - \overline{E}_\alpha) d\mathbf{R}}{\int |\Psi|^2 d\mathbf{R}} \\
&\quad - \frac{\int 2\Psi\Psi_\alpha d\mathbf{R} \int |\Psi|^2 (E_L - \overline{E})^2 d\mathbf{R}}{(\int |\Psi|^2 d\mathbf{R})^2} \\
&= 2\left[\langle E_{L,\alpha}(E_L - \overline{E}) \rangle_{|\Psi|^2} - \overline{E}_\alpha \langle E_L \rangle_{|\Psi|^2} + \overline{E}_\alpha \overline{E} \right. \\
&\quad \left. + \left\langle \frac{\Psi_\alpha}{\Psi} (E_L^2 - 2E_L\overline{E} + \overline{E}^2) \right\rangle_{|\Psi|^2} + \left\langle \frac{\Psi_\alpha}{\Psi} \right\rangle_{|\Psi|^2} \langle (E_L^2 - 2E_L\overline{E} + \overline{E}^2) \rangle_{|\Psi|^2} \right]
\end{aligned}$$

$$\begin{aligned}
(\sigma^2)_\alpha = 2 \Bigg[& \langle E_{L,\alpha}(E_L - \overline{E}) \rangle_{|\Psi|^2} + \left\langle \frac{\Psi_\alpha}{\Psi} E_L^2 \right\rangle_{|\Psi|^2} - \left\langle \frac{\Psi_\alpha}{\Psi} \right\rangle_{|\Psi|^2} \langle E_L^2 \rangle_{|\Psi|^2} \\
& - 2\overline{E} \left\langle \frac{\Psi_\alpha}{\Psi} (E_L - \overline{E}) \right\rangle_{|\Psi|^2} \Bigg]
\end{aligned}$$

By ignoring the change of the wave function with respect to free parameters, and alternative expression can be written.[51] Thus, a fixed set of Monte Carlo configurations can be used to compute the variance.

$$(\sigma^2)_\alpha = 2 \left\langle E_{L,\alpha}(E_L - \overline{E}) \right\rangle_{|\Psi|^2} = 2 \left\langle (E_{L,\alpha} - \overline{E}_\alpha)(E_L - \overline{E}) \right\rangle_{|\Psi|^2} \tag{A.5}$$

For the Hessian matrix elements, using Levenberg-Marquardt approximation, the

Hessian matrix can be obtained as

$$(\sigma^2)_{\alpha\beta} = 2\left\langle (E_{L,\alpha} - \overline{E}_\alpha)(E_{L,\beta} - \overline{E}_\beta)\right\rangle_{|\Psi|^2} \tag{A.6}$$

APPENDIX B

EXPONENTIAL REPRESENTATION OF TRIAL WAVE FUNCTIONS

In order to simplify the implementation and calculation of derivatives of the trial wave functions, an exponential representation is used in VMC and DMC context.

The trial wave function is defined as (dropping the T subscript indicating the "trial")

$$\Psi = e^J D \text{ where } D = \sum_i c_i \text{det} A_i^{\uparrow} \text{det} A_i^{\downarrow}, \tag{B.1}$$

A_i^{σ} is the ith Slater determinant with spin σ and J is the Jastrow factor. However, we can represent it in exponential form as the following.

$$\Psi = e^{\varphi} \text{ where } \varphi = \ln(e^J D) = \ln(\exp(J)) + \ln(D) \tag{B.2}$$

Equation B.2 allows us to calculate the derivatives without extra effort on chain rules and products. The first spacial derivative of the trial wave function becomes

$$\begin{aligned} \nabla\Psi &= \nabla e^{\varphi} \\ &= (\nabla\varphi)e^{\varphi} \end{aligned} \tag{B.3}$$

The second derivative is

$$\begin{aligned} \nabla^2\Psi &= \nabla[(\nabla\varphi)e^{\varphi}] \\ &= (\nabla^2\varphi)e^{\varphi} + (\nabla\varphi)\cdot(\nabla\varphi)e^{\varphi} \\ &= \left(\nabla^2\varphi + |\nabla\varphi|^2\right)e^{\varphi} \end{aligned} \tag{B.4}$$

The representation in equation B.2 makes it more clear to calculate the necessary quantities e.g. $\nabla\Psi/\Psi$ and the local energy E_L.

$$\frac{\nabla\Psi}{\Psi} = \nabla\varphi \tag{B.5}$$

$$\frac{\nabla^2\Psi}{\Psi} = \left(\nabla^2\varphi + |\nabla\varphi|^2\right) \tag{B.6}$$

$$\begin{aligned} E_L &= \frac{\hat{H}\Psi}{\Psi} \\ &= \frac{1}{\Psi}\left(-\frac{1}{2}\nabla^2\Psi + V\Psi\right) \\ &= -\frac{1}{2}\left(\nabla^2\varphi + |\nabla\varphi|^2\right) + V \end{aligned} \tag{B.7}$$

APPENDIX C

LEAKY GAUSSIAN BASIS FUNCTION AND ITS DERIVATIVES

Implementation of a new basis function requires the derivatives of the basis function with respect to free parameters (for VMC optimization), and the gradient and the laplacian of the basis function (for VMC and DMC). We define the following notations in order to have simple forms for the complicated derivatives.

$$\begin{aligned} r_x &= x - x_0, \\ r_y &= y - y_0, \\ r^2 &= r_x^2 + r_y^2 \end{aligned} \tag{C.1}$$

$$g = \exp(-\alpha r^2/2), \;\; h = 1 - \beta r^2, \;\; \text{where } \alpha > 0, \; \beta \geq 0 \tag{C.2}$$

$$f = gh \tag{C.3}$$

C.1. Main derivatives

$$\frac{\partial}{\partial x} f = g r_x \left(-\alpha h - 2\beta\right) \tag{C.4}$$

$$\frac{\partial}{\partial y} f = g r_y \left(-\alpha h - 2\beta\right) \tag{C.5}$$

$$\nabla^2 f = g\left(4\alpha\beta r_x^2 + 4\alpha\beta r_y^2 + \alpha h\left(\alpha r_x^2 - 1\right) + \alpha h\left(\alpha r_y^2 - 1\right) - 4\beta\right) \tag{C.6}$$

$$= g\left(4\alpha\beta r^2 + \alpha h\left(\alpha r^2 - 2\right) - 4\beta\right) \tag{C.7}$$

$$= g\left(\alpha h\left(\alpha r^2 - 2\right) + 4\beta\left(\alpha r^2 - 1\right)\right) \tag{C.8}$$

C.2. Derivatives with respect to x_0

$$\frac{\partial}{\partial x_0} f = g r_x \left(\alpha h + 2\beta\right) \tag{C.9}$$

$$\frac{\partial}{\partial x_0}\frac{\partial}{\partial x_0} f = g\left(4\alpha\beta r_x^2 + \alpha h\left(\alpha r_x^2 - 1\right) - 2\beta\right) \tag{C.10}$$

$$\frac{\partial}{\partial x_0}\frac{\partial}{\partial y_0} f = -\alpha g r_x r_y \left(-\alpha h - 4\beta\right) \tag{C.11}$$

$$\frac{\partial}{\partial x_0}\frac{\partial}{\partial \alpha} f = \frac{g r_x \left(-\alpha h r^2 - 4\beta r^2 + 2\right)}{2} \tag{C.12}$$

$$\frac{\partial}{\partial x_0}\frac{\partial}{\partial \beta} f = -g r_x \left(\alpha r^2 - 2\right) \tag{C.13}$$

$$\frac{\partial}{\partial x_0}\frac{\partial}{\partial x}f = g\left(-\alpha^2 h r_x^2 - 4\alpha\beta r_x^2 + \alpha h + 2\beta\right) \tag{C.14}$$

$$\frac{\partial}{\partial x_0}\frac{\partial}{\partial y}f = \alpha g r_x r_y\left(-\alpha h - 4\beta\right) \tag{C.15}$$

$$\begin{aligned}\frac{\partial}{\partial x_0}\nabla^2 f = \alpha g r_x \Big(&4\alpha\beta r_x^2 + 4\alpha\beta r_y^2 + \alpha h\left(\alpha r_x^2 - 1\right) + \alpha h\left(\alpha r_y^2 - 1\right) \\ &-2\alpha h + 2\beta\left(\alpha r_x^2 - 1\right) + 2\beta\left(\alpha r_y^2 - 1\right) - 12\beta\Big) \qquad \text{(C.16)} \\ = \alpha g r_x \Big(&4\alpha\beta r^2 + \alpha h\left(\alpha r^2 - 2\right) - 2\alpha h + 2\beta\left(\alpha r^2 - 2\right) - 12\beta\Big) \qquad \text{(C.17)} \\ = \alpha g r_x \Big(&-2\alpha h + 2\beta\left(\alpha r^2 - 2\right) - 8\beta\Big) + \alpha r_x \nabla^2 f \qquad \text{(C.18)}\end{aligned}$$

C.3. Derivatives with respect to y_0

$$\frac{\partial}{\partial y_0}f = g r_y\left(\alpha h + 2\beta\right) \tag{C.19}$$

$$\frac{\partial}{\partial y_0}\frac{\partial}{\partial y_0}f = g\left(4\alpha\beta r_y^2 + \alpha h\left(\alpha r_y^2 - 1\right) - 2\beta\right) \tag{C.20}$$

$$\frac{\partial}{\partial y_0}\frac{\partial}{\partial x_0}f = -\alpha g r_x r_y\left(-\alpha h - 4\beta\right) \tag{C.21}$$

$$\frac{\partial}{\partial y_0}\frac{\partial}{\partial \alpha}f = \frac{g r_y \left(-\alpha h r^2 - 4\beta r^2 + 2\right)}{2} \tag{C.22}$$

$$\frac{\partial}{\partial y_0}\frac{\partial}{\partial \beta}f = -g r_y \left(\alpha r^2 - 2\right) \tag{C.23}$$

$$\frac{\partial}{\partial y_0}\frac{\partial}{\partial x}f = \alpha g r_x r_y \left(-\alpha h - 4\beta\right) \tag{C.24}$$

$$\frac{\partial}{\partial y_0}\frac{\partial}{\partial y}f = g\left(-\alpha^2 h r_y^2 - 4\alpha\beta r_y^2 + \alpha h + 2\beta\right) \tag{C.25}$$

$$\begin{aligned}\frac{\partial}{\partial y_0}\nabla^2 f = \alpha g r_y \Big(&4\alpha\beta r_x^2 + 4\alpha\beta r_y^2 + \alpha h\left(\alpha r_x^2 - 1\right) + \alpha h\left(\alpha r_y^2 - 1\right) \\ &-2\alpha h + 2\beta\left(\alpha r_x^2 - 1\right) + 2\beta\left(\alpha r_y^2 - 1\right) - 12\beta\Big) \qquad \text{(C.26)} \\ = \alpha g r_y \Big(&4\alpha\beta r^2 + \alpha h\left(\alpha r^2 - 2\right) - 2\alpha h + 2\beta\left(\alpha r^2 - 2\right) - 12\beta\Big) \qquad \text{(C.27)} \\ = \alpha g r_y \Big(&-2\alpha h + 2\beta\left(\alpha r^2 - 2\right) - 8\beta\Big) + \alpha r_y \nabla^2 f \qquad \text{(C.28)}\end{aligned}$$

C.4. Derivatives with respect to α

$$\frac{\partial}{\partial \alpha}f = -\frac{g h r^2}{2} \tag{C.29}$$

$$\frac{\partial}{\partial\alpha}\frac{\partial}{\partial\alpha}f = \frac{ghr^4}{4} \tag{C.30}$$

$$\frac{\partial}{\partial\alpha}\frac{\partial}{\partial x_0}f = \frac{gr_x\left(-\alpha hr^2 - 4\beta r^2 + 2\right)}{2} \tag{C.31}$$

$$\frac{\partial}{\partial\alpha}\frac{\partial}{\partial y_0}f = \frac{gr_y\left(-\alpha hr^2 - 4\beta r^2 + 2\right)}{2} \tag{C.32}$$

$$\frac{\partial}{\partial\alpha}\frac{\partial}{\partial\beta}f = \frac{gr^4}{2} \tag{C.33}$$

$$\frac{\partial}{\partial\alpha}\frac{\partial}{\partial x}f = -\frac{gr_x\left(-\alpha hr^2 - 4\beta r^2 + 2\right)}{2} \tag{C.34}$$

$$\frac{\partial}{\partial\alpha}\frac{\partial}{\partial y}f = -\frac{gr_y\left(-\alpha hr^2 - 4\beta r^2 + 2\right)}{2} \tag{C.35}$$

$$\begin{aligned}\frac{\partial}{\partial\alpha}\nabla^2 f &= g\left(\alpha hr_x^2 + \alpha hr_y^2 + 4\beta r_x^2 + 4\beta r_y^2 + h\left(\alpha r_x^2 - 1\right) + h\left(\alpha r_y^2 - 1\right)\right. \\ &\quad \left. + \frac{r^2\left(-4\alpha\beta r_x^2 - 4\alpha\beta r_y^2 - \alpha h\left(\alpha r_x^2 - 1\right) - \alpha h\left(\alpha r_y^2 - 1\right) + 4\beta\right)}{2}\right) \qquad \text{(C.36)} \\ &= g\left(\alpha hr^2 + 4\beta r^2 + h\left(\alpha r^2 - 2\right) + \frac{r^2\left(-4\alpha\beta r^2 - \alpha h\left(\alpha r^2 - 2\right) + 4\beta\right)}{2}\right) \qquad \text{(C.37)} \\ &= g\left(\alpha hr^2 + 4\beta r^2 + h\left(\alpha r^2 - 2\right)\right) - \frac{r^2\nabla^2 f}{2} \qquad \text{(C.38)}\end{aligned}$$

C.5. Derivatives with respect to β

$$\frac{\partial}{\partial \beta} f = -gr^2 \tag{C.39}$$

$$\frac{\partial}{\partial \beta}\frac{\partial}{\partial \beta} f = 0 \tag{C.40}$$

$$\frac{\partial}{\partial \beta}\frac{\partial}{\partial x_0} f = -gr_x \left(\alpha r^2 - 2\right) \tag{C.41}$$

$$\frac{\partial}{\partial \beta}\frac{\partial}{\partial y_0} f = -gr_y \left(\alpha r^2 - 2\right) \tag{C.42}$$

$$\frac{\partial}{\partial \beta}\frac{\partial}{\partial \alpha} f = \frac{gr^4}{2} \tag{C.43}$$

$$\frac{\partial}{\partial \beta}\frac{\partial}{\partial x} f = gr_x \left(\alpha r^2 - 2\right) \tag{C.44}$$

$$\frac{\partial}{\partial \beta}\frac{\partial}{\partial y} f = gr_y \left(\alpha r^2 - 2\right) \tag{C.45}$$

$$\frac{\partial}{\partial\beta}\nabla^2 f = g\left(-\alpha r^2\left(\alpha r_x^2 - 1\right) - \alpha r^2\left(\alpha r_y^2 - 1\right) + 4\alpha r_x^2 + 4\alpha r_y^2 - 4\right) \tag{C.46}$$

$$= g\left(-\alpha r^2\left(\alpha r^2 - 2\right) + 4\alpha r^2 - 4\right) \tag{C.47}$$

$$= g\left(-\alpha r^2\left(\alpha r^2 - 6\right) - 4\right) \tag{C.48}$$

APPENDIX D

SINGLE PARTICLE SCHRÖDINGER EQUATION SOLUTION IN 2D USING FINITE DIFFERENCE METHOD

In order to solve single particle Schrödinger Equation (SPSE) numerically, the differential operators in SPSE is expanded using a finite difference scheme. SPSE in effective atomic units (electronic charge e, dielectric constant ϵ, effective mass m^*, and $\hbar$ are set to 1) is

$$-\frac{1}{2}\frac{\partial^2}{\partial x^2}\Psi(x,y) - \frac{1}{2}\frac{\partial^2}{\partial y^2}\Psi(x,y) + V(x,y)\Psi(x,y) = E\Psi(x,y) \tag{D.1}$$

with $\Psi(x,y) = 0$ while $x \to \infty$ and $y \to \infty$. Since we try to solve it numerically, we need to choose a 2D box of length L by L with Dirichlet boundary conditions $\Psi = 0$ at boundaries. L should be much larger than the effect of the potential profile so that numerical solution converges without errors.

Using central finite difference formula two times on differential operators, equation D.1 can be approximated as

$$-\frac{1}{2}\frac{\Psi_{i+1,j} - 2\Psi_{i,j} + \Psi_{i-1,j}}{h^2} - \frac{1}{2}\frac{\Psi_{i,j+1} - 2\Psi_{i,j} + \Psi_{i,j-1}}{h^2} + V_{i,j}\Psi_{i,j} = E\Psi_{i,j} \tag{D.2}$$

where x and y axis are equally discretized into N partitions so that $\Delta x = \Delta y = L/N = h$. The grid is $N \times N$ where $i = 0, 1, ..., N-1$, $j = 0, 1, ..., N-1$, and $\Psi_{0,j} = \Psi_{N-1,j} = \Psi_{i,0} = \Psi_{i,N-1} = 0$.

If the left hand side (LHS) of equation D.2 can be written as a matrix H the solutions are equivalent to finding eigenvalues and eigenvectors of matrix H ($H\Psi = E\Psi$). In order to transform equation LHS of D.2 into a matrix, let us rearrange equation D.2 as

$$\left(\frac{2}{h^2} + V_{i,j}\right)\Psi_{i,j} + \left(-\frac{1}{2h^2}\right)(\Psi_{i+1,j} + \Psi_{i-1,j} + \Psi_{i,j+1} + \Psi_{i,j-1}) = E\Psi_{i,j} \tag{D.3}$$

Equation D.3 is valid only for points not on the boundary. In order to incorporate this equation into a finite difference system so that it has a matrix form, 2D grid should be mapped into a 1D index as

$$m = (i-1) \times (N-1) + (j-1) \text{ for } i = [1, N-2] \text{ and } j = [1, N-2] \tag{D.4}$$

Mapping of the 2D indices in equation D.3 is the following.

- $(i, j) : m = (i-1) \times (N-1) + (j-1)$
- $(i-1, j) : m_{\text{left}} = (i-2) \times (N-1) + (j-1)$
- $(i+1, j) : m_{\text{right}} = (i) \times (N-1) + (j-1)$
- $(i, j-1) : m_{\text{bottom}} = (i-1) \times (N-1) + (j-2)$
- $(i, j+1) : m_{\text{top}} = (i-1) \times (N-1) + (j)$

Using this mapping equation D.3 becomes

$$\left(\frac{2}{h^2} + V_m\right)\Psi_m + \left(-\frac{1}{2h^2}\right)(\Psi_{m_{\text{right}}} + \Psi_{m_{\text{left}}} + \Psi_{m_{\text{top}}} + \Psi_{m_{\text{bottom}}}) = E\Psi_m \tag{D.5}$$

The matrix H can be constructed using equation D.5 as the following.

1. For central point (i, j), Ψ_m:

$$H[m, m] = \frac{2}{h^2} + V_m$$

2. For right neighbor $(i+1, j)$, $\Psi_{m_{\text{right}}}$:

$$H[m, m_{\text{right}}] = -\frac{1}{2h^2}$$

3. For left neighbor $(i-1, j)$, $\Psi_{m_{\text{left}}}$:

$$H[m, m_{\text{left}}] = -\frac{1}{2h^2}$$

4. For top neighbor $(i, j+1)$, $\Psi_{m_{\text{top}}}$:

$$H[m, m_{\text{top}}] = -\frac{1}{2h^2}$$

5. For bottom neighbor $(i, j+1)$, $\Psi_{m_{\text{bottom}}}$:

$$H[m, m_{\text{bottom}}] = -\frac{1}{2h^2}$$

Therefore, the matrix elements of H for row $(i, j) : m$ by incorporating the boundary conditions

$$H[m,:] = \begin{cases} -\frac{1}{2h^2} & \text{at column } (i+1, j) : m_{\text{right}} \text{ if } i+1 \neq N-1 \\ -\frac{1}{2h^2} & \text{at column } (i-1, j) : m_{\text{left}} \text{ if } i-1 \neq 0 \\ -\frac{1}{2h^2} & \text{at column } (i, j+1) : m_{\text{top}} \text{ if } j+1 \neq N-1 \\ -\frac{1}{2h^2} & \text{at column } (i, j-1) : m_{\text{bottom}} \text{ if } j-1 \neq 0 \\ \frac{2}{h^2} + V_m & \text{at column } (i, j) : m \\ 0 & \text{otherwise} \end{cases} \tag{D.6}$$

Since H is only valid for interior points, the matrix size is $N-1 \times N-1$. Eigenvalues are energies, and eigenvectors are the corresponding solutions given by a 1D vector. After finding the eigenvectors, 2D grid can be constructed by applying equation .

APPENDIX E

EFFECTIVE ATOMIC UNITS

The effective atomic units can vary across different materials. Given that many components of atomic units are material-dependent, it is essential to account for these variations. The most important quantities are effective mass of the electrons m^* and the dielectric constant κ for a given material. Additionally, Landé g-factor g^* should be known if there are calculations related to magnetism. In the following sections, atomic unit calculations are given.

E.1. Atomic unit of length

Bohr radius is given as

$$a_0 = \frac{4\pi\varepsilon_0\hbar^2}{m_e e^2} = 5.291772109 \times 10^{-11}\ \text{m} \tag{E.1}$$

where ε_0 is the vacuum permitivity, $\hbar$ is the reduced Planck's constant, m_e is the mass of the free electrons and e is the charge of the electrons. For calculation of atomic units, we multiply the given value of Bohr radius by the ratios of the electric permitivity and the electron masses instead of calculating whole equation in order to preserve the numerical accuracy as much as possible. Let us define ratio of the effective mass of the electrons inside the material relative to the free electron mass as

$$m_r = \frac{m^*}{m_e} \tag{E.2}$$

On the other hand, the dielectric constant, or the relative permitivity, is already the ratio of the permitivity of the material ε relative to the vacuum permivitivy ε_0, and expressed

as

$$\kappa = \frac{\varepsilon}{\varepsilon_0} \tag{E.3}$$

If the Bohr radius a_0 is multiplied by κ/m_r, the effective Bohr radius is obtained as below.

$$\begin{aligned} a_0^* &= a_0 \frac{\kappa}{m_r} \\ &= \frac{4\pi\varepsilon_0\hbar^2}{m_e e^2} \frac{\varepsilon}{\varepsilon_0} \frac{m_e}{m^*} = \frac{4\pi\varepsilon\hbar^2}{m^* e^2} \end{aligned} \tag{E.4}$$

Thus, the effective atomic unit of length is

$$a_0^* = a_0 \frac{\kappa}{m_r} \tag{E.5}$$

The conversion of a length ℓ to atomic units for a given material is the following.

$$\ell^* = \frac{\ell}{a_0^*} \tag{E.6}$$

Therefore, using equation E.5;

$$\ell^* = \ell \left(a_0 \frac{\kappa}{m_r} \right)^{-1} \tag{E.7}$$

E.2. Atomic unit of energy

The atomic unit of energy, the Hartree energy, can be expressed as

$$E_h = m_e \left(\frac{e^2}{4\pi\varepsilon_0\hbar} \right)^2 = 27.211386245988 \text{ eV} \tag{E.8}$$

The effective Hartree energy for a given material can be calculated via multiplying the Hartree energy by m_r/κ^2, where $m_r = m^*/m_e$ and $\kappa = \varepsilon/\varepsilon_0$.

$$\begin{aligned} E_h^* &= E_h \frac{m_r}{\kappa^2} \\ &= m_e \left(\frac{e^2}{4\pi\varepsilon_0\hbar}\right)^2 \frac{m^*}{m_e} \left(\frac{\varepsilon_0}{\varepsilon}\right)^2 = m^* \left(\frac{e^2}{4\pi\varepsilon\hbar}\right)^2 \end{aligned} \tag{E.9}$$

Thus, the effective atomic unit of energy is

$$E_h^* = E_h \frac{m_r}{\kappa^2} \tag{E.10}$$

The conversion of an energy E to atomic units for a given material is the following.

$$E^* = \frac{E}{E_h^*} \tag{E.11}$$

Therefore, using E.10;

$$E^* = E \left(E_h \frac{m_r}{\kappa^2}\right)^{-1} \tag{E.12}$$

APPENDIX F

NAGAOKA FERROMAGNETISM

Nagaoka ferromagnetism, first predicted by Nagaoka[35] within the framework of Hubbard model, is a strongly correlated state where a single hole in a half-filled lattice induces a fully spin-polarized configuration. In order to invoke this state, the Coulomb interaction between the electrons in the same site should diverge. The Hubbard Hamiltonian is

$$H = -t \sum_{\langle i,j \rangle,\sigma} c^{\dagger}_{i\sigma} c_{j\sigma} + U \sum_{i} c^{\dagger}_{i\uparrow} c_{i\uparrow} c^{\dagger}_{i\downarrow} c_{i\downarrow} + h.c. \tag{F.1}$$

where $c^{\dagger}$ (c) is the creation (annihilation) operator, t is the hopping parameter between nearest neighbor sites, U is the Coulomb interaction between the electrons in the same site, and $\langle i, j \rangle$ indicates the sum is over nearest neighbor indices. There are three conditions required to have Nagaoka ferromagnetism.

• If there are N sites, and N_e electrons, there should be exactly one hole, $N_e = N - 1$.

• There should be strong correlation between electrons, $U \to \infty$. Double occupancy is not allowed.

• The connectivity condition: All spin configurations in a S_Z (z component of total spin) subspace should be connected to each other by a single hopping of the hole to the nearest neighbor site (i.e. all possible spin configurations can be generated from any configuration with nearest-neighbor hopping of the single hole in the system.).

Nagaoka ferromagnetism can be understood from a different perspective, as well. Consider a single hole in an example system of 5×5 lattice as shown in Fig. F.1. The Coulomb interaction goes to infinity, i.e. two electrons are not allowed to be in the same site. If the system is in a fully spin polarized state, the hole can move to anywhere (by a nearest-neighbor hopping) since all electrons have the same spin. The hole is distributed to whole lattice, the kinetic energy is small. If the state is AFM, the spin order should be

preserved. The hole cannot move to all sites in the lattice by preserving the spin structure. The movement of the hole is restricted, thus the kinetic energy increases. If the system is in a partially polarized state, the hole is less restricted than AFM case, but the local spin order in the lattice should be preserved again. The movement of the hole is more restricted than FM case. The kinetic energy is higher than the fully polarized state. Therefore, the FM state is the ground state with the smallest kinetic energy.

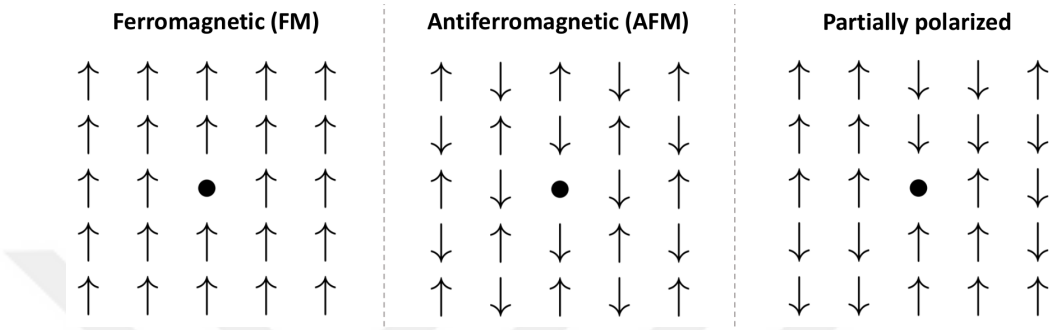

Figure F.1. Demonstration of a single hole in a 5×5 lattice in several spin configurations.

The Nagaoka ferromagnetism can be induced when there is an extra electron in the system.[35] Additionally, it is proven with more generalized (and finite) Coulomb interactions by Tasaki.[36]

VITA

Gökhan Öztarhan

EDUCATION

2019 - 2025: Doctor of Philosophy in Physics

İzmir Institute of Technology, İzmir, Turkey

Thesis Title: Quantum Monte Carlo Study of Semiconductor Artificial Graphene Nanostructures

Advisor: Prof. Dr. A. Devrim Güçlü

2015 - 2018: Master of Science in Physics

İzmir Institute of Technology, İzmir, Turkey

Thesis Title: Quantum Monte Carlo Study of the Multi-Orbital Anderson Model Including the SU(2) Invariant Hund's Coupling

Advisor: Prof. Dr. Nejat Bulut

2009 - 2015: Bachelor of Physics

İzmir Institute of Technology, İzmir, Turkey

PROFESSIONAL EXPERIENCE

2020 - Present: Research and Teaching Assistant

Department of Physics, İzmir Institute of Technology, İzmir, Turkey

PUBLICATIONS FROM THIS THESIS

• Öztarhan, G.; Kul, E. B.; Okcu, E.; Güçlü, A. D. Quantum Monte Carlo study of semiconductor artificial graphene nanostructures. Phys. Rev. B 2023, 108, L161114.

• Öztarhan, G.; Potasz, P.; Güçlü, A. D. Nagaoka ferromagnetism in semiconductor artificial graphene. arXiv, 2025.